PRELIMINARY INDIRECT MEASUREMENT OF COSMIC-RAY PROTON SPECTRUM USING EARTH'S γ-RAY DATA FROM *FERMI* LARGE AREA TELESCOPE

PATOMPORN PAYOUNGKHAMDEE

A THESIS SUBMITTED IN PARTIAL FULFILLMENT
OF THE REQUIREMENTS FOR
THE DEGREE OF MASTER OF SCIENCE (PHYSICS)
FACULTY OF GRADUATE STUDIES
MAHIDOL UNIVERSITY
2021

Thesis
entitled

.....
Mr. Patomporn Payoungkhamdee
Candidate

.....
Asst. Prof. Warit Mitthumsiri,
Ph.D. (Physics)
Major advisor

.....
Prof. David Ruffolo,
Ph.D. (Physics)
Co-advisor

.....
Dr. Alejandro Sáiz,
Ph.D. (Physics)
Co-advisor

.....
Prof. Patcharee Lertrit,
M.D., Ph.D. (Biochemistry)
Dean
Faculty of Graduate Studies
Mahidol University

.....
Assoc. Prof. Kittiwit Matan,
Ph.D. (Physics)
Program Director
Master of Science Program in Physics
(International Program)
Faculty of Science
Mahidol University

Thesis
entitled

was submitted to the Faculty of Graduate Studies, Mahidol University
for the degree of Master of Science (Physics)
on
May 18, 2020

.....
Mr. Patomporn Payoungkhamdee
Candidate

.....
Assoc. Prof. Paisan Tooprakai,
Ph.D. (Physics)
Chair

.....
Asst. Prof. Warit Mitthumsiri,
Ph.D. (Physics)
Member

.....
Prof. David Ruffolo,
Ph.D. (Physics)
Member

.....
Prof. Patcharee Lertrit,
M.D., Ph.D. (Biochemistry)
Dean
Faculty of Graduate Studies
Mahidol University

.....
Assoc. Prof.P̃alangpon Kongsaree,
Ph.D. (Organic Chemistry)
Dean
Faculty of Science
Mahidol University

ACKNOWLEDGEMENTS

Thanks to the members of space physics laboratory..

Patomporn Payoungkhamdee

PRELIMINARY INDIRECT MEASUREMENT OF COSMIC-RAY PROTON SPECTRUM USING EARTH'S γ-RAY DATA FROM *FERMI* LARGE AREA TELESCOPE.

PATOMPORN PAYOUNGKHAMDEE 5736149 SCPY/D

M.Sc. (PHYSICS)

THESIS ADVISORY COMMITTEE: WARIT MITTHUMSIRI, Ph.D. (PHYSICS), DAVID RUFFOLO, Ph.D. (PHYSICS), ALEJANDRO SÁIZ, Ph.D. (PHYSICS)

ABSTRACT

Cosmic rays (CRs) are high-energy particles, mostly protons, propagating in space. The rigidity (momentum per charge) spectrum of CRs is well described by a power law for which the spectral index is approximately 2.8 around 30 - 1000 GV. Recent measurements by PAMELA and AMS-02 indicate an abrupt change of the CR proton spectral index at about 340 GV. When CRs interact with the Earth's upper atmosphere, γ rays can be produced and detected by space-based detectors. Here we use the Earth's γ-ray data collected by the *Fermi* Large Area Telescope along with a proton-air interaction model to indirectly determine the CR proton spectral index and compare against observations by other instruments.

KEY WORDS: COSMIC RAYS / EARTH'S GAMMA RAYS

73 pages

CONTENTS

CONTENTS (cont.)

LIST OF TABLES

LIST OF FIGURES

CHAPTER I
INTRODUCTION

1.1 Overview

Space is full of fascinating phenomena, why stars are bright to more advanced questions such as whether dark matter exists. Human curiosity has brought us so far that now we can observe the sky with more sophisticated techniques. However, the research to gather new knowledge by studying the space is endless. The answer to one question sometimes generate another mystery. Research in physical science also helps creating new technology because of the need to overcome challenging limitations of the instruments or techniques.

The frontier of astrophysical research is continually expanding over time because the exploration of one thing does open the new door to another dark room which has been waiting for human to shine a light to explore. There are various branches in astrophysics from theoretical foundation, simulation and experimental physics which all compliment each other for pushing the frontier of the human knowledge. To study high energy particle accelerators in the universe, the possibility of direct probing of multiple Galactic sources which produce high-energy particles, or cosmic rays (CRs), is nearly impossible in terms of current technology and resources required. Nevertheless, the technology of observing the particles arriving the Earth is more plausible for scientists.

CRs can be observed with two types of detectors: ground-based and spaced-based. Analyzing and studying CR data allows us to interpret properties of their sources and cosmic environment.

The spectrum of CRs follows a power law with different spectral indices depending on the rigidity (momentum per charge) range of particles. There are multiple types of CR sources in space including unknown sources. There are multiple types of CR sources in space including unknown sources. Consequently,

changing of the spectral index from one rigidity to another rigidity will find the discontinuity if there is the translation from one source type to another source from the superposition of multiple spectrums.

Fermi-LAT has been launched into the sky and orbiting around the Earth and looking around the space in γ-rays regions. It found that the ring of brightness around the Earth's limb where the major factor that causes this phenomenon is the interaction of incoming CRs with the Earth's upper atmosphere as analyzed in Abdo et al. (2009). Then the spectrum of γ-rays that was induced by the incoming CRs are highly related to the spectrum of CRs.

The first indirect measurement was conducted with 5 years of observations and indicate that there is a breaking of spectral index around 302 GV with a significant level 1 σ. The significant level at this stage is not so strong to conclude the study. The reasons probably came from the nature of the CRs if there is no discontinuity in the incident CRs spectrum, the indirect could measurement distort the information so that the sign could be reducing or the exposure time during the observations is still not enough. To confirm that we did our best on the data collection side, performing the analysis with more data could also put us out of doubt for the last clue.

1.2 Objectives

The objectives of this study are to

- To indirectly measure the cosmic ray proton spectrum in rigidity range gigaelectronvolt (GV)
- To put the weight on the previous study with more dataset
- To improve the optimizaiton technique by using heuristical methodology
- To reduce the calculation time by inventing a whole new parallel code in low level from scratch

1.3 Outline of Thesis

The dissertation would provide the various information from the overview introductory context to the technical detail employ in this study as well as the result and interpretation. It is structured as follows.

Chapter I will introduce the reader to the overview of the long track from the historical analogy and zooming into the specific branch of research to get the reader to see where we are and what we are doing to fulfill the frontier of the research.

Chapter II is the background knowledge that will be used in this study. This chapter also has a brief of history in cosmic ray research community which contains an important finding and the impactful experiment that brings us to this far in the research field. Some theoretical detail will be provided on par with the historical discovery but the subchapter of the specific topic will describe more detail in the depth of astroparticle physics that involving the high energy physics. Not only the concept of physical process but this chapter also has the apparatus information where the majority of the content covering the detector part in the spacecraft to demonstrate how the apparatus gather the γ-rays data.

Chapter III is mainly consist of multiple literature reviews involving the study to clarify the theoretical idea as well as for filling the fundamental concept that takes the reader to understand the next chapter in detail.

Chapter IV would cover the article reviewing. The content is staring from the pioneering article of the field and the evolution that inspire this work.

Chapter V consists of datasets selection, flux calculation , problem optimization and interpretation.

CHAPTER II
BACKGROUND

2.1 Cosmic-ray

This section consists of historical discovery, from the origin of this field of study until the latest impactful experiment. Not only historical content, but it also contains the physical explanation with the phenomenon that involving the CR research.

2.1.1 History

In 1909, the famous experiment that pioneer the study of CR has been led by Theodor Wolf who takes conduct the experiment of altitude variation by taking the apparatus to measure the rate of ionization from the ground to the top of the Eiffel Tower in Paris (Gray (1949)). The result showed that there the ionization rate was slightly increased when the altitude is higher which gives clues that the origin of cosmic rays was coming from outer space rather than Earth's inner shell. Hörandel (2013)

However, the experiment of measuring the effect of altitude variation with a tiny altitude scale compared to the Earth's atmosphere would not enough to consolidate the theory. In the same year, the ballon with a similar instrument has been released up to 1.3 kilometers by Karl Bergwitz to put more weight on the first experiment. They found that the ionization has increased by a quarter compared to ground level (De Angelis (2014)). Three years later, the suicidal investigation was conducted by an Australian gentleman who brought the detector and himself to fly with the balloon. His name is Victor Hess, people might have no doubt why this the name went so famous because he risks his life with the experiment and he was flying over 5 kilometers above the ground (Hess (1912)). The result is strongly significant and impactful to the astrophysical research community. Risking life In

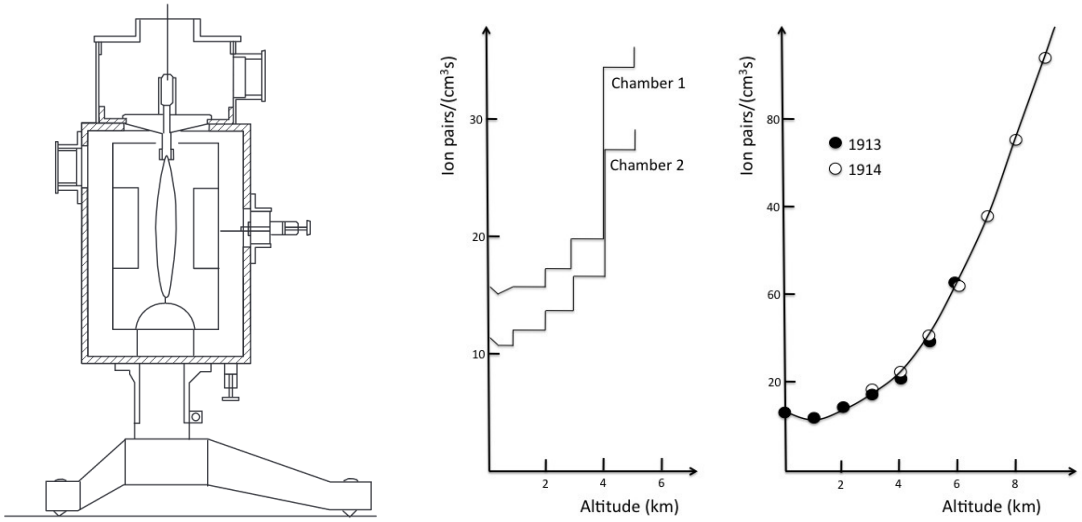

(a) An early version schematic view of electrometer used by Thedor Wulf (Hörandel (2013))

(b) Ionizaiton rate from Victor Hess (left) and Werner Kolhörster (right)

Figure 2.1: Wulf's apparatus and the ballon experimental results

1914, Werner Kolhörster repeated the balloon experiment with a higher altitude which around 9 kilometers from the sea level and the ionization rate still does increase when the ballon flew higher. This emphasizes that the source of those ionizing ray came from Earth's upper atmosphere or the outer space.

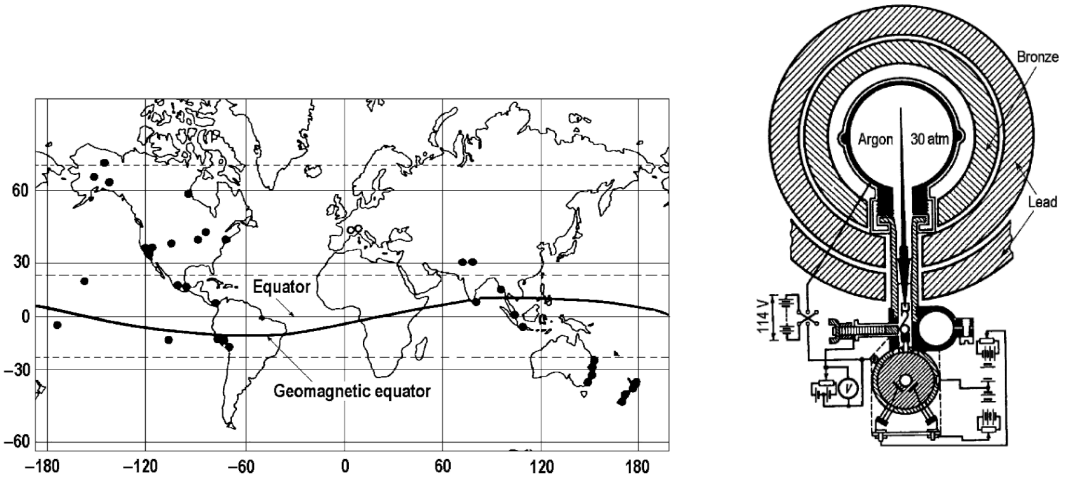

(a) Main points where CR intensities were measured during eight Compton expeditions in 1932

(b) The Pb-shielded ionization chamber, organized by Compton (Dorman (2009))

Figure 2.2: Clay Experiment of geographical variation

Not only the altitude variable that related to the the intensity of the CRs,

but the geographic location of the observation also does affect the measurement. The first experiment has done by John Clay who sailed the ship across the ocean from Holland to Java (Clay (1927, 1928)). The geographical locations that are used to measure the CR intensities and the apparatus schematical draft is shown in Figure 2.2. The result shows that the further from the equator, the higher CR intensity. Another exploration for the geographic variation was done by John Compton in the following five years. He sailed the ship from Sydney (northern hemisphere) to Vancouver (the southern hemisphere) for various season during 1936 to 1937 back and forth (Compton & Turner (1937)). The Figure 2.3 demonstrates the latitude variation and the seasonality effects of the multiple trips from the experiment.

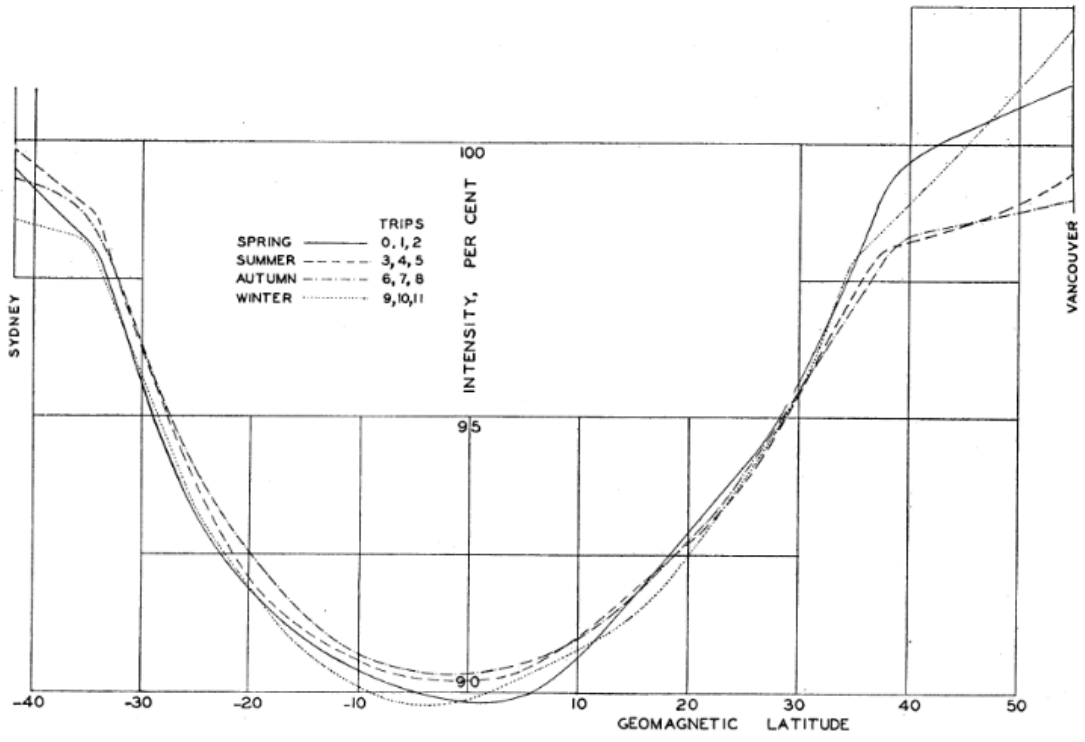

Figure 2.3: Latitude variation for various seasons (Compton & Turner (1937))

The first interpretation study from the discovery has been done by Carl Störmer. The explanation of the CR's altitude variation came from the trajectory of CR particles due to geomagnetic field (Störmer (1934)). In that period, the topic of the geomagnetic field and the effects of CRs was quite famous. Another

impactful study of the CRs trajectory and the relevant of Earth's magnetic field was conducted by Bruno Rossi for predicting an asymmetry of the East-West distribution of CR spectrum because the primary CRs does have a positive or the negative charge than the cyclic moving direction of the the particle was induced by Lorentz force where the direction of the Earth's magnetic field could be identified to determine the direction of the charged particles (Rossi & Greisen (1941)).

A ground-based detector is a great option for detecting the CRs where it includes primary and secondary CRs. However, investigating the primary CRs is a challenging topic for ground-based detectors especially for low energy particles. Another interesting option to inspect the asymmetry of East-West could be done by using a space-based detector that orbit around the Earth's at some radius in the the higher altitude and it would face a lower the atmospheric density which considers to be an interesting the choice to study the CRs with a lower effect of atmospheric interaction. In 2008, *Fermi* Large Area Telescope (LAT) has been launched to observed γ-ray and lightweight lepton particles which are electron and position. The East-West effects from geomagnetic induction was also emphasized by *Fermi*-LAT.

2.1.2 Physical properties

CRs are high-energy particles that propagating through space. The momentum of the particles came from various acceleration mechanisms base on where it from such as supernovae, active galactic nuclei, quasars, and gamma-ray bursts. The composition of CRs consists of 90% protons, 8% alphas, and other nuclei of heavier elements (Dembinski et al. (2017)). Experimentally, many observations indicate that the spectrum of CRs for all particles and individually does follow the power law in rigidity (momentum per charge) with a specific spectral index depends on their energy range. Theoretically, the observed spectrum with a broad energy range would represent the superposition of arrival CRs with a diverse producer where each producer has its specific character which is the spectral index. By the end of the day, it is barely possible to distinguish the origin of CR particles one by one. Then it is more plausible to provenance the origin of CR particles in the

macroscale rather than inspecting in the microscale.

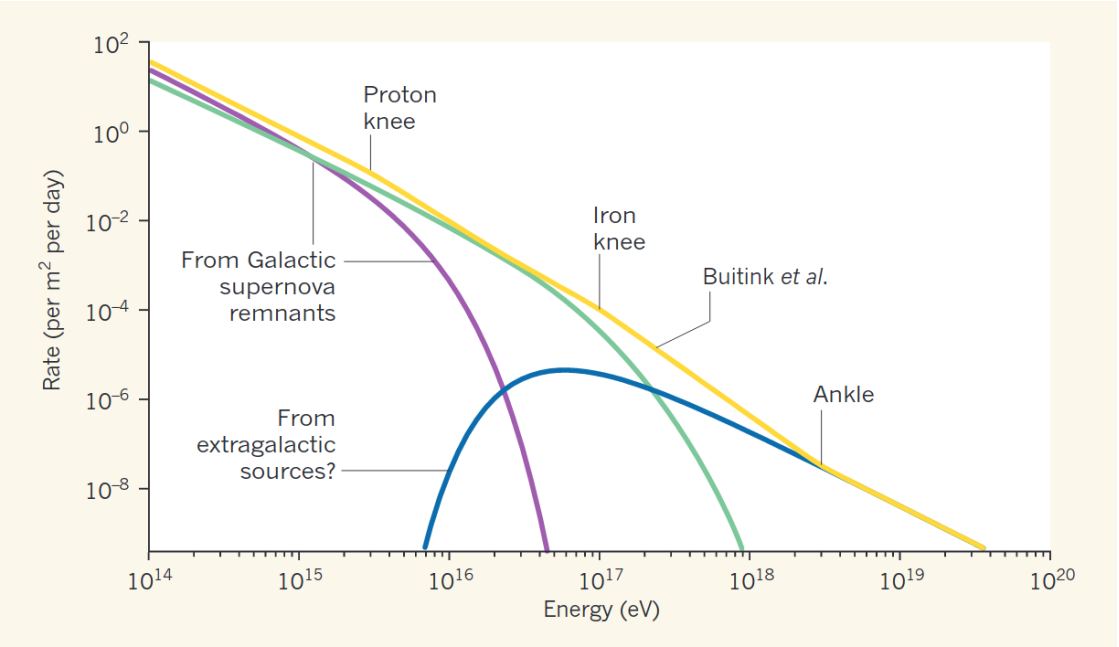

Figure 2.4: Superposition of CR spectrum (Taylor (2016))

As mentioned in an early paragraph, each source of CR does reflect their own specific spectral index in the arrival CR spectrum. To validate the theoretical assumption, putting the simulation or calculation of each source and check with the real data does compliment experimental observations. The superposition of various sources that yield a discontinuity of the spectral indices has been exploited in some energy ranges. Two well-known breaking points are knee and ankle where it located in the energy order around 10^{15} eV and 10^{18} eV sequentially. Approximately, the rate to find one particle at the knee is around one particle per square meter per year and the possibility that the apparatus could detect the particle in energy at ankle point is roughly one particle per kilometer per year. Figure 2.4 illustrate the concept of superposition from various sources and yield the arrival CR spectrum with breaking spectral indices.

Not only the below ankle energy that has an interesting property, but the CR that has energy beyond the ankle energy also has an identical property. It knowns as "ultra-high energy cosmic rays" (UHECR). One interesting point is that it does not that far from the ankle in terms of rigidity magnitude which

higher around 1 or 2 order of magnitude. The widely known explanation why it could not go so far is the Greisen–Zatsepin–Kuzmin limit (GZK limit). The theory provides the description of why the UHECR could not propagate though the space but please note that some sources still could produce such a UHECR but the main the issue here it the space does not empty. It contains some intermediate matter or dust and the microwave background radiation which it is believed that came from the residue of the Big Bang or some great explosion or expansion of the space that human never saw it (at least in the human lifetime). The main calculation of the CR kinetic energy limit from GZK was considered only proton particles and the main interaction that makes it stop is basically from the interaction with microwave background radiation that almost perfectly isotropically propagating in the space with an order of traveling proton around hundred light-years in the space (Greisen (1966)). The way of this kind of interaction not only does slow down the CR proton by producing neutral pion where it mostly decays into a pair of γ-rays but it could also yield a neutron with a charged pion. Hence, it also answers why we could see such a high energy neutron that does not only produced in the sky (shower effects) albeit it does not has any charge to be accelerated in the famous acceleration mechanism such as shock acceleration.

The types of CRs could be divided into two kinds based on how they were produced which are

1. **Primary cosmic rays**: they mostly are produced from the Solar system, somewhere in the Milky ways, extragalactic sources and many more. When they interact with the Earth's atmosphere, with the hadronic interaction with the air molecules, they produce the secondary CR particles.

2. **Secondary cosmic rays**: as mentioned in collapsing of the primary CRs, secondary CRs consists of many particles from lightweight leptons to medium weight leptons and from mesons to hadron particles as well. The interaction of the proton with the atmospheric molecule looks simple but the precise calculation from derivation is extremely complicated since there is the endless possibility of the (Feynman) path that also produce other products with a

certain probability. By the end of the day, we got a few certain of particles from their likelihood of the occurrence from the collision which mainly are electrons, positions, muons, pions and photons as demonstrates in Figure 2.5.

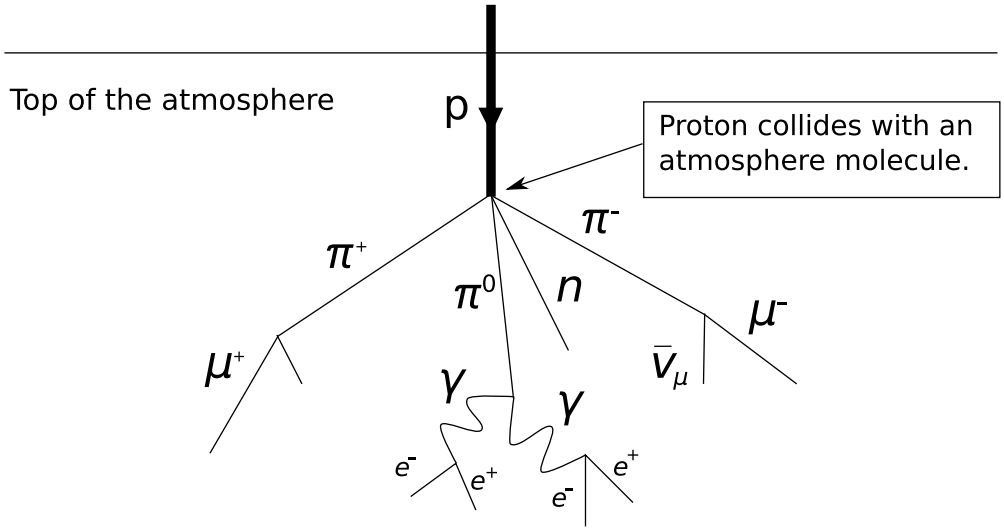

Figure 2.5: Cosmic rays shower from collision of primary CR with the atmospheric molecule

2.1.3 γ-ray production

The production of γ-ray particles happens all the time. It is mandatory to understand how a photon could gain a very high momentum from nature. The procedure to acquire all those kinetic energies is quite different from how a charged particle obtains its momentum because a the charged particle could earn their kinetic energy during their trip of propagating through space with a Lorentzian force. The γ-rays mostly have only one chance to pick their kinetic energy and it happens when it was produced because it is barely interact with any other particles in the space especially high energy γ-ray. The scenarios that make photon hold high energy are listed in the following bullets.

Mechanism of γ-ray producing

- **Decaying of unstable matter**: Radioactive decay is one of the most well-known phenomena for the γ-decay mode. One example of heavy-ion decay is

cobalt-60. It decays into an excited state of nickel as

$$^{60}_{27}\mathrm{Co} \longrightarrow {}^{60}_{28}\mathrm{Ni}^{*} + \mathrm{e}^{-} + \bar{\nu} + \gamma\,,$$

then the excited nickel decay another γ-ray to make it to the stable state

$$^{60}_{28}\mathrm{Ni}^{*} \longrightarrow {}^{60}_{28}\mathrm{Ni} + \gamma\,.$$

The famous decay of a lower level from a small nucleus that consists of two quarks called "meson". To be more precise, it is known as the pion decay. The path diagram is demonstrated in Figure 2.6 where the neutral pion from the collision process that interacts via Yukuwa's interaction. The neutral pion itself does not stable then it would have a short amount of lifetime before it mostly decays into two high-energy photons. Neutral pion also could

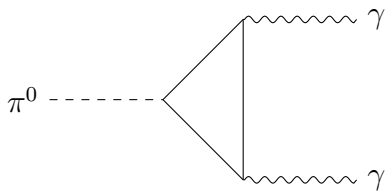

Figure 2.6: Feynman's diagram of neutral pion decays into two γ-rays

yield one γ-ray and a pair of lightweight leptons, a couple pair of lightweight leptons or even just a pair of lightweight leptons and much more as long as it conserve the momentum, energy and quantum numbers. The main reason why the majority of their decaying process does yield only photons because the scattering amplitude as the Figure 2.6 does hold a branching ratio around 0.98823 and the rest of them are smaller than 1%. Another interesting property of this decay mode is the momentum vector of their pair γ-ray hold an opposite direction with the same amplitude in the reference frame.

- **electron–positron annihilation**: In the universe, there is some probability of the electron and position was forced to face each other by some chance from the electromagnetic force or randomly found each other. The interaction when they facing each other dominate by electromagnetic interaction and requires a photon as a mediator to allow them to talk to each other from

a quantum electrodynamics point of view. There is a change when those pair of leptons decide to annihilate into high energy photons without running any physical laws. Nevertheless, another kind of a pair of leptons like muon technically could deform into two photons with much higher energy because their rest mass is higher. Surely, a pair of Tau is also allowed to produces a pair of photons. However, the lifetime of those medium-weight and heavy-weight leptons could not last that long to survive in practical. The simplest Feynman's path of annihilation of leptons into a pair of photons is illustrated in Figure 2.7 from light to heavy leptons sequentially.

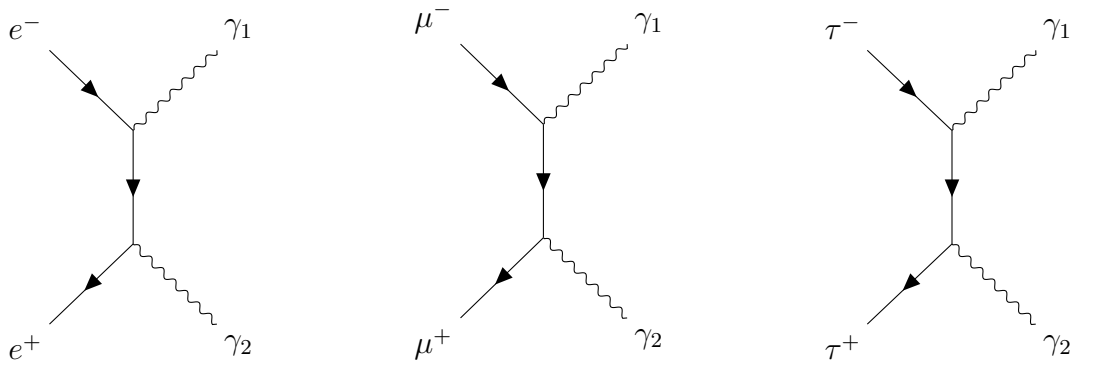

(a) Lightweight leptons (b) Mediumweight leptons (c) Heavyweight leptons

Figure 2.7: Major lepton annihilation path diagram

- **Synchrotron radiation& Bremsstrahlung radiation**: The phenomena of turning the momentum direction of charged particles or accelerate into another direction share a similar description. Conservation of momentum has come into place when considering the bending charged particle that would emit the photon. Regarding the incoming direction of a charged particle and then turning it direction by $\pi/2$ radians. The question that comes into mild is where does those initial momentum in an the incoming direction does since the momentum is conserved along the cartesian direction, not only the magnitude. Now the clue is here, they have to emit the photon to converse the momentum of the system.

  Let walk through the first example called synchrotron radiation. Keeping

some charged particle circulating the donut-like apparatus have some cost to pay to make them stay without escaping the tunnel. Unquestionably, dragging some moving particle circulating at some point requires a centripetal force. In this case, applying electromagnetic force without touching it would yield a radiation called synchrotron emission.

The second mechanism is Bremsstrahlung, where a charged particle or typically an electron moving path close to some opposite charged particle or typically a proton. The explanation from Coulomb's law would cover this scheme for the definition that the force is inverse proportional to the distance between two charges. Then moving past by an oppositely charged particle does induce the electron bending and emit the photon because the explained reason from the previous paragraph. This mechanism happens when CR electrons moving through the matter of the Sun's chromosphere and interact with a positive charged and produce some high energy photon but usually it produces in the X-ray energy range.

Mechanism of γ-ray gaining momentum

Even though, γ-ray usually does not prefer to talk to other fundamental particles because scattering amplitude of their interaction is pretty low. Nonetheless, there are some scenarios that γ could gain more kinetic energy and losing their kinetic energy when they traveling in the universe.

- **Inverse Compton scattering** The scattering of a photon (massless particle) with an electron (massive particle) could occur during their trip. Equation 2.1 demonstrate the symbolic relation of the scattering with the electromagnetic interaction and yield the same particles as an incoming particles.

$$e^{-}\gamma \rightarrow e^{-}\gamma \tag{2.1}$$

Interaction between an electron and a photon could make them converting the momentum via the scattering process. Since the system momentum has

to be conserved, then there will be one losing momentum and another one gaining momentum or kinetic energy. Suppose one photon is traveling and hits an electron or a charged particle, it could transfer the kinetic energy to the particle and their wavelength will be longer. In another word, it is losing kinetic energy. On the other hand, this scenario could happen oppositely. There is a situation when a high energy electron interacting with the photon and turns over its kinetic energy to the photon. After that, a photon could gain more kinetic energy during their trip. The latter scenario is called "Inverse Compton Scattering". The most likelihood choice of the interaction of the scheme could be represented in Feynman's path as in Figure 2.8.

(a) First branch (b) Second branch

Figure 2.8: Trivial Feynman's path of (Inverse) Compton scattering

γ-ray production plants

- **Supernova ramnants (SNRs) and molecular cloud**: The supernova explosion is a huge expansion from that approximately expanding as a spherical shell that sweep the interstellar medium (ISM) and decelerate at some radius after the enlargement. The kinetic energy that transfers from the momentum in the radial axis was modeled and believed to be the kinetic energy of the cosmic ray particles. Three major processes involves in this phenomenon which are nuclear pion production, nonthermal electron bremsstrahlung, and Compton scattering (Dermer & Powale (2013)). Last but not least, shock acceleration could play an important role in this phenomenon.

- **Diffused γ-ray emission from galactic plane**: One of the bright sources that do not locate too far from our territory is the galactic plane. The first

reasonable explanation is the distance of the productive objects does not far from Earth comparing to other extragalactic sources. In addition, there are many interesting CR sources in our galaxy. It might be a pulsar, some flare of the event of an explosion and so on. The plot that shows the brightness of the galactic plane comparing to outer space is shown in Figure 2.9.

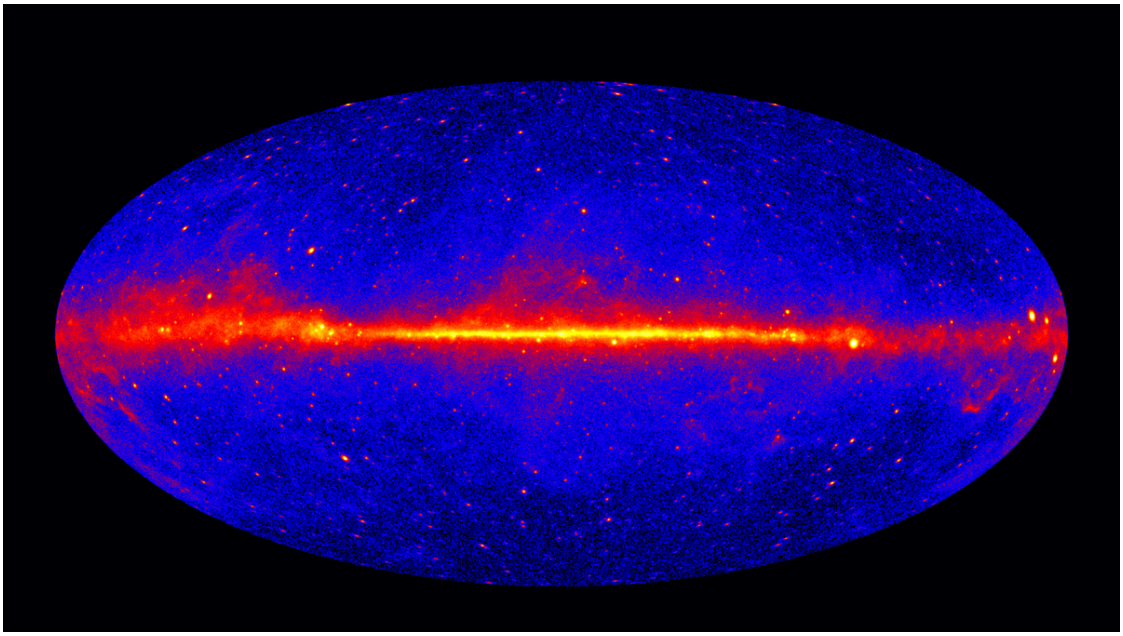

Figure 2.9: Intensity of γ-ray > 1 GeV in galactic coordinate (Image credit: NASA/DOE/*Fermi* LAT Collaboration)

- **Pulsar and Active Galactic Nucleus (AGN)**: Another source of the brightness in Figure 2.9 is the bright dots with a different solid angle width in the sky. The majority of those spots consists of γ-ray from pulsar's periodic emission and AGN or extremely luminous AGN namely "Quasar". The cycle of the lighthouse effects from pulsar is very robust as in the scale of an atomic clock. Both of them has a very high magnetic field strength. Emissive photons from those sources would be very high energy due to the accelation of a charged particle near magnetic poles or the outer.

- **Earth's limb γ-ray production**: The closest γ-ray source is our Earth's atmosphere. To be more precise, the Earth's upper atmosphere is super bright in γ-ray exposure. The main reason that causes the shining of Earth's limb does come from the collision of the CR's massive particle such as protons

and alphas. The interaction of those high energy CR massive particles yields many more particles and main contribution of the γ-ray dazzling came from the neutral pion decay which is the product of the collision process.

2.2 *Fermi* Large Area Telescope (LAT)

One of the famous space telescopes that do see the sky in the visible wavelength is *Fermi* Large Area Telescope (LAT). Formerly, it was called Gamma-ray Large Area Space Telescope (GLAST). The mission of the satellite is to collect high energy photon data or γ-ray and it technically could detect the lightweight lepton particles namely electron and position. The orbiting radius is around 550 kilometers from sea level. It is designed for observing the full-sky in γ-ray region. It also attaches the Gamma-ray Burst Monitor (GBM) to study gamma-ray bursts for seeking an exotic event. The telescope was launched in 11 June 2008 at 16:05 UTC or 21:05 Bangkok time by abroad with Delta II 7920-H rocket.

2.2.1 Overview

According to Figure 2.10, each component of the *Fermi* telescope was designed for a purpose since there is no ideal detector module that could detect kind of particles. There are two main parts where the first part is the major component called Large Area Telescope (LAT) for detecting the γ -ray and the second part is Gamma-ray Burst Monitor (GBM) for seeking an interesting event in the sky. Both of them do detect the γ-ray but in the different energy scale. LAT is the main component where it detects the γ-ray in a few dozen of GeV up to a digit of TeV. For the GBM part, the visible photon energy for them is around 8 keV to 40 MeV. The GBM consists of two sub components which are sodium iodide detector for low-energy photons (8 keV to 1 MeV) and bismuth germanate detector for high-energy photons (0.2 MeV to 40 Mev). GBM detectors distribute around the telescope to be a closed circuit camera and looking for a flare of the γ-ray. The actual purpose of GBM is not a detector for collecting a high quality data but it is

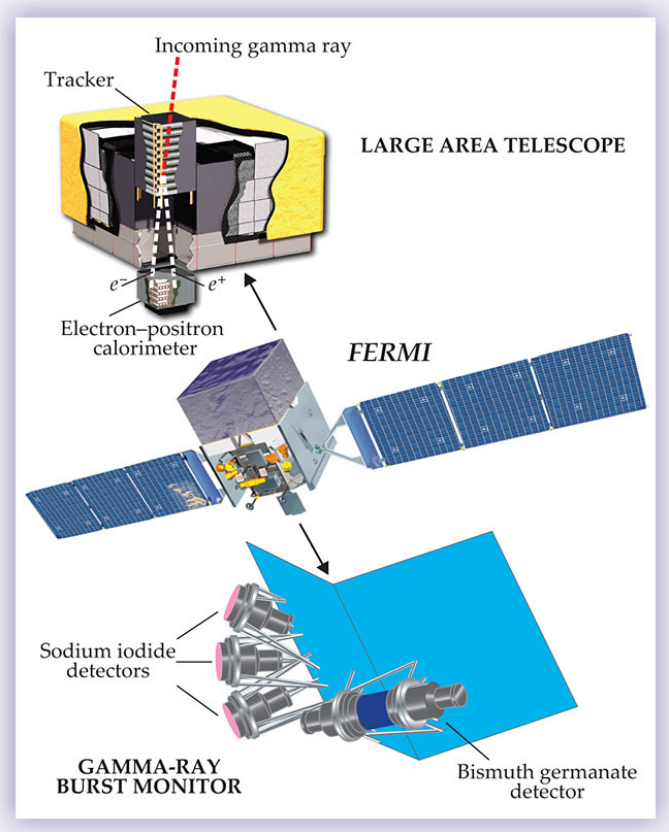

Figure 2.10: Main components of *Fermi*-LAT (Image taken from Michelson et al. (2010))

attached in the spacecraft to assist the LAT in mainly looking at an interesting event that could produce a huge amount of γ-rays. The content in this chapter will deep down into more detail of LAT depth and would not provide more detail of GBM.

2.2.2 Large Area Telescope (LAT)

LAT consists of a tracker (TKR) module for tracing the incoming photon, calorimeter (CAL) for measuring the kinetic energy after the particle has been passed through the tracker because a charged particle interact with the CAL and dissipate since it enters the module and anti-coincidence Detector (ACD) for rejecting the background signal. The last part is the onboarding data acquisition (DAQ) module for investigating the particle's footprint and digitize the signal.

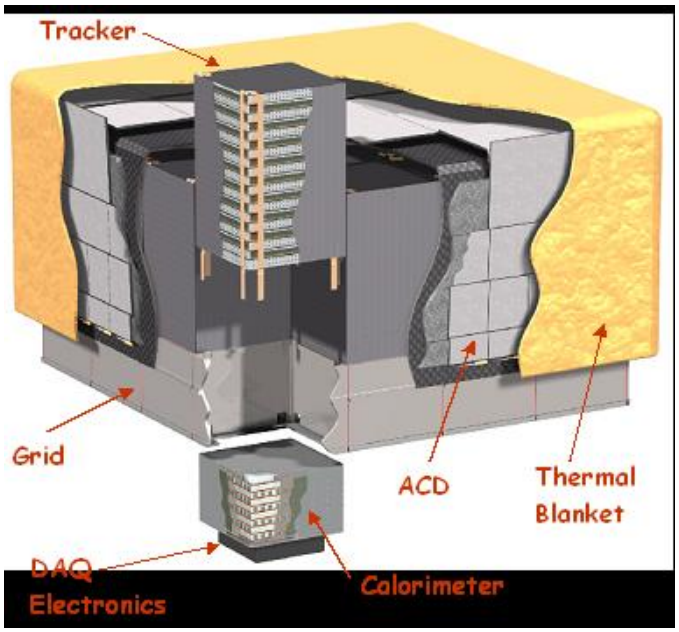

Figure 2.11: Instrument structure (Image taken from https://fermi.gsfc.nasa.gov)

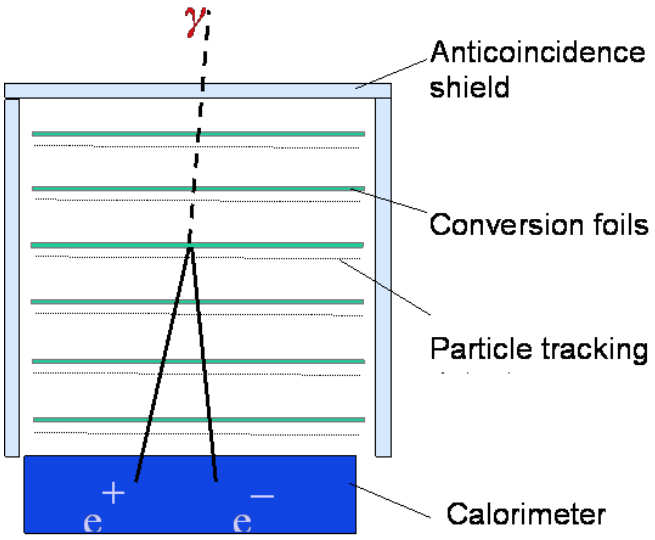

Figure 2.12: Schematic structure of the LAT (Image taken from https://fermi.gsfc.nasa.gov)

Tracker

Higher energy photon or γ-ray talk to the LAT by converting the kinetic energy into a pair of lightweight leptons or e^+e^- pair. The converter-tracker has 16 planes of a large atomic number for making the incident γ-ray convert into a pair of e^+e^- as demonstrated in Figure 2.12. After that, a pair of leptons would leave a footprint as an electromagnetic induction in particle tracker where it sensitive for

the moving charged particle.

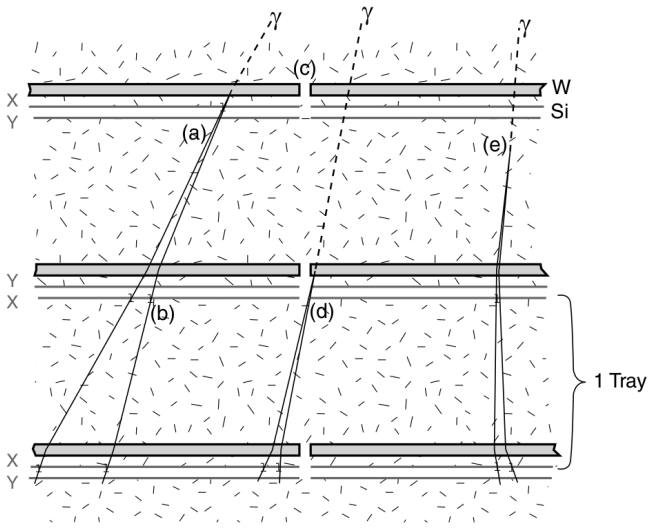

Figure 2.13: LAT's particle tracker (Image taken from Atwood et al. (2009))

The particle tracking is made from silicon strips. Tracking information would leave the track in a 2-D plane of particle tracking. In order to traceback and gaining data as the 3-D moving direction, 16 particle tracker has to be taken into account for constructing the electron or positron path. Despite one layer of particle tracking could obtain the information about incoming leptons for x-y plane only, but technical design of LAT does put 2 layers of the silicon-based tracker with a very narrow gap between them. This kind of design could make the LAT performing measurement precision in the angular resolution better than a single layer of a wide gap which affects the point-spread function (PSF) of the probability distribution from reconstruction direction. According to Figure 2.13, the top and the bottom of silicon trackers and the heavy-nuclei conversion layer called "Tray". Case (a) and (b) in the figure is the ideal case where the γ-ray hit the conversion layer and multiple footprints are recorded. Nevertheless, there is an edge case as in (d) and (e) where the γ-ray has a probability to skip an early layer and choose to covert in the secondary conversion layer and will be detected in the upcoming tracking layer. The major benefit of deploying multiple conversion layers are quite obvious for a better event gathering.

Calorimeter

Unlike particle tracker that talks to a charged particle by utilizing the EM induction without (or barely) disturbing the particle state, the calorimeter is a starving component. It consumes a lepton and produce electronic readout of the energy from the radiation of the lepton in the crystal scintillator. The size of this part is mainly considered from the radiation lengths of the electron and position particles becasue it has to record the shower that happens during the decaying process. However, the radiation length highly depends on the kinetic energy of the particle. The LAT itself has been designed for detecting photon energy range between MeV to a few hundred GeV. Hence, the exposure of photon energy beyond TeV is probably not promising in this case.

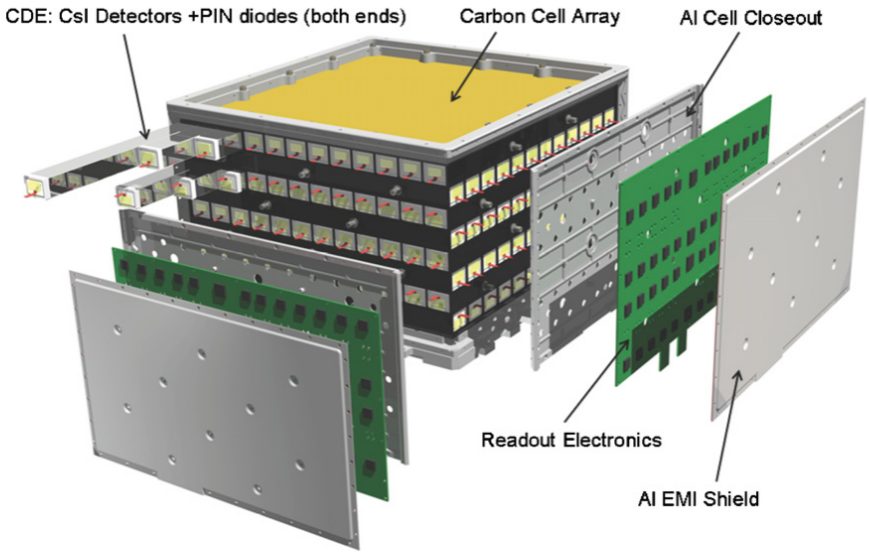

Figure 2.14: LAT's calorimeter (Image taken from Atwood et al. (2009))

The overview apparatus structure is illustrated in Figure 2.14. Each calorimeter module consists of 96 CsI(Tl) scintillator crystal size 2.7 cm x 2.0 cm x 32.6 cm and PIN photodiodes at both ends which connect to the readout electronic components for translate an amount of light that has been sparked in the crystal to digitized signal. Each horizontal layer is combined from 12 crystal component and stack them 8 times by rotate them 90°each for boosting the angular resolution from the sparking lights. The carbon cell was build for supporting the structure of low

mass particle tracker due to the properties of high stiffness, thermal conductivity and thermal stability. An electron, position, or γ-ray will deposit the energy in the calorimeter as the scintillated lights via electromagnetic interactions. The segmented crystal also allows LAT to trace the shower as the spatial imaging.

Anti-coincidence Detector (ACD)

The main objective of ACD is to support the charged-particle background rejection of the CRs. It is cover the tracker over the LAT field of view (FoV) for 4 sides and the top part of the LAT. It consists of 89 plastic scintillator tiles with 5×5 array on top and 4 sides of 16 tiles. Each tile component contains two photomultiplier and wanelength shifting fibers embedded in the scintillator. The tile is overlapping another one in one dimension to reduce the effect of the gaps between them. To be more precise, there are two sets of four called scintillator ribbons for covering the top-down side and a pair around their center. The ACD is required to has 0.9997 efficientcy for detecting an incoming charged particle of FoV of the LAT. However, the γ-ray induces the shower that the calorimeter will absorb but there is a scenario called the "backsplash effect" where the secondary particles in keV range from the electromagnetic shower could interact with the incoming photon and Compton scattering in ACD. Then it could create a veto signal from the recoil electron. To solve this issue, the ACD with their neighborhood would take the incident candidate photon into account and could dramatically reduce the effect of the back splashing.

Data Acquisition System (DAQ)

To acquire an interesting event, event selection could not be done on software on the ground level from the whole raw signal of subsystems because of the limitation of the hardware in the current edge. To collect an event, raw data will be selected from the filtering algorithm on board. The hierarchical structure of data acquisition system (DAQ) was invented for seeking a transient event as shown in Figure 2.15.

The lowest level is tower electronic modules (TEMs) to serve as an

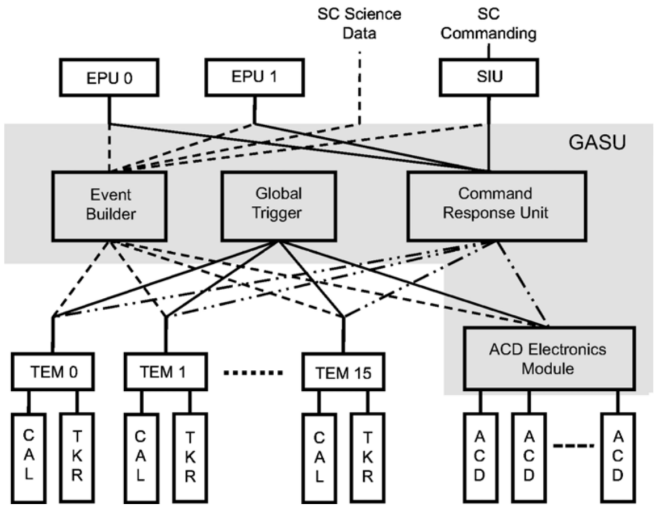

Figure 2.15: Flow chart of LAT's data acquisition system (DAQ) (Image taken from Atwood et al. (2009))

interface for the tracker and calorimeter. All TEMs create an event buffering and communicates with the Event Builder Module (EBM) which is a component of Global-trigger/ACD-module/Signal Distribution Unit (GASU). Command Response Unit (CRU) was built to communicate the software execution in the DAQ system. Lastly, the Event Processing Unit (EPU) will process a selecting event from TEM and ACD Electronics Module (AEM). Filtering an event could reduce the information flowing rate from a few kHz to around 400 Hz which will be sent back to the ground level.

2.2.3 Event reconstruction

In an early day, the reconstruction algorithm for tracing a photon is Monte Carlo (MC) simulation. Modeling the incident γ-rays and the background has been simulated in the orbiting-like environment before it launches. Meaning that background rejection property already embedded in the LAT since the developing process. The simulation could be use for the detector calibration since the simulation software provide an interactive physical process.

The main logic of the reconstruction is to start by tracking the footprint in the tracker and expect the output in the calorimeter cube as physical process would yield. After that, the event classification mainly consider from the ACD part

to classify an event type.

The result from processed data on the fly is level 0 and it will pass down to Earth and reconstructing the photon data called level 1. The more LAT orbiting around the Earth's, the more understanding of the LAT environment and it brings the software improvement for the reconstruction algorithm to exploit the technique of pattern recognition. The first official release is LAT data is Pass 6 and Pass 7 after has been released with the same level 0 data but the reconstructed event is more efficient than the older one by software level. The newest version and likely to be the final version is Pass 8. Not only the reconstruction algorithm that has been divided but the event class is also an crucial concept. As mentioned earlier, the photon is classified into a specific class. There is no free lunch to think that the detector see the particle as a binary classification. It will mix with a likelihood or probability to distinguish the specific kind of interesting event. That is the main reason why *Fermi*-LAT team split the event into multiple classes which mainly are TRANSIENT, SOURCE, ULTRACLEAN and ULTRACLEANVETO.

Lesser photon candidates have been selected in the ULTRACLEANVETO. Then there is no certain right or wrong for picking the class from the researcher's point of view. The main criteria would be the objectives of the analysis. If the analyzer wants to collect as much events as possible and could accept some noisy event, then SOURCE or TRANSIENT class is suitable for the analysis and vice versa.

2.2.4 Detector performance and their characteristics

Fermi-LAT has been designed for detecting γ-ray in the space which means that the range of energy that it could see precisely will be starting at MeV up to TeV. The effective area in square-meters is defined from the front and the back of the LAT's tracking layer by considering the upper part as a front and the bottom part belowing a certain layer as the back part. Since both front and back part components are made by the same materials and exactly the same design. Then total effective area could be sum into a single value. Figure 2.16 visualize the effectiveness of LAT along with a given energy range. According to the plot, LAT

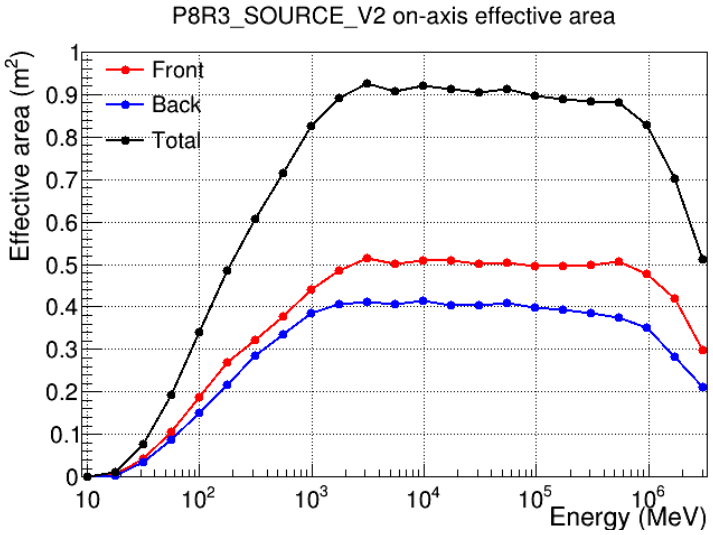

Figure 2.16: Effective area along the photon energy range from MeV to TeV (Maldera (2019))

performs a measurement well from GeV up to TeV scale.

Another crucial part when dealing with LAT effectiveness is the incidence angle (θ_{LAT}). It highly affects the number of tracking layers. The higher probability of passing more tracking layers would yield a better LAT's performance. Figure 2.17 shows relation of effective area versus incidence angle.

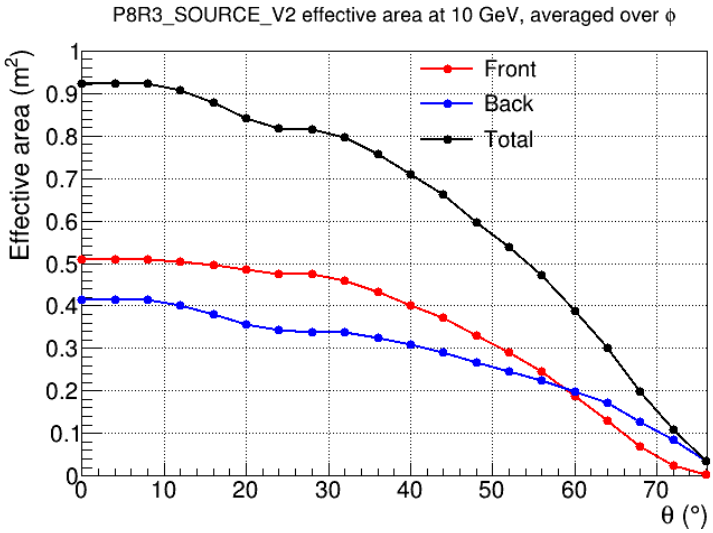

Figure 2.17: Effective area versus incidence angle (Maldera (2019))

Imagine the LAT structure as a cube-like detector. Surely, the LAT boresight is a square where an azimuthal angle (ϕ_{LAT}) of the incoming photon

would affect a larger area that the photon could interact as demonstrates in Figure 2.17. The reason why there is a peak for any cycle of $\pi/2$ radian or 90°is the edge of the LAT would have more area to interact than the lateral. Another evidence for the explanation is the front effective area has fewer effects since the propagation length is narrow than the back.

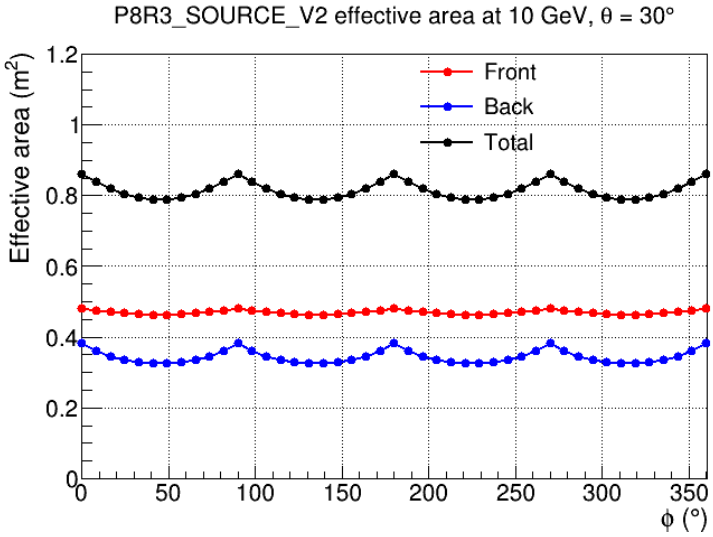

Figure 2.18: Effective area versus azimuthal angle (Maldera (2019))

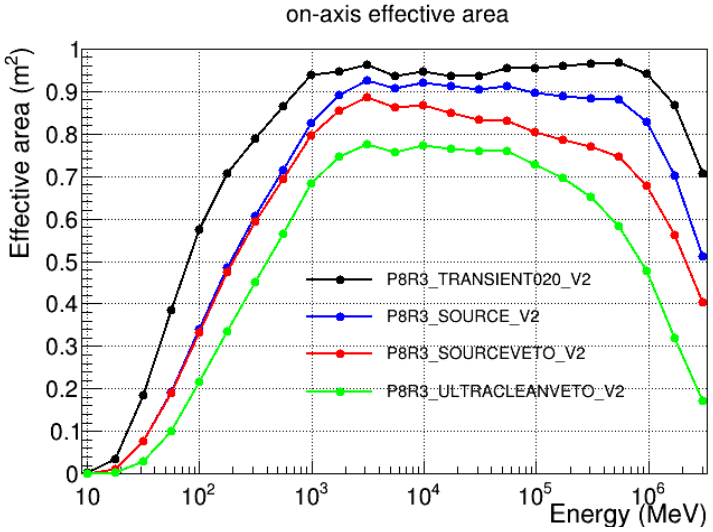

Figure 2.19: Effective area along the energy of each event class (Maldera (2019)))

From the previous subsection, the event class also plays a crucial role when considering the effectiveness of the reconstructed event. Undoubtedly, the cleanest class namely "ULTRACLEANVETO" would have the worst effective area.

In opposite, the TRANSIENT class would yield the best effective area as visualized in Figure 2.19.

To sum up, the effective area act for the LAT performance for seeking an event in the unit of square lengths. It also behaves like a function in the practical analysis which pragmatically allows the client to throw incidence angle, azimuthal angle and the energy. Then it will return the effective area in a unit of square centimeters in the raw format.

CHAPTER III
LITERATURE REVIEW

Cosmic-ray could come from different origins from galactic sources to extra-galactic sources. The kinetic energy of cosmic rays also highly depends on where does it from. Low energy CRs usually came from the Sun called "solar energetic particle". The production process of soalr particle event mostly came from the coronal mass ejection (CME) when HZE ions were dragged by a magnetic field in the plasma. The extra-galactic CRs typically has high momentum from the extreme condition of the acceleration mechanism in pulsar, quasars and supernova remnant (SNR). The theoretical description of acceleration in SNR and solar flares is the shock wave acceleration in the following paragraph.

One of the most impactful studies of CR's acceleration mechanism was conducted by Fermi (1949). The study describes how high energy CR particle gain such a huge momentum from the shock wave that was generated by supernovae or a great explosion from the heavy dense star. How it gains the kinetic energy could be described as a first-order shock acceleration and the overall spectrum of charged particles could be represented as the power law in Equation 3.1.

$$\frac{dN(E)}{dE} \propto E^{-\gamma} \tag{3.1}$$

where $\gamma \geq 2$ in the non-relativistic regime. However, moving magnetized plasma cloud can accelerate the charged particle in the space called "second-order Fermi acceleration". Both regimes were computed the Lorentzian forces regardless of thermal collision in the process.

The CR protons are major components in the arrival of CR particles under multiple observations. However, α-particle is also a second important CR particle when considering a precise calculation of CR interactions. The other majority of heavy weight nuclei that could propagate through space are C, O,

Ne and so on. The differential flux in kinetic energy of multiple observations is visualzed in the Figure 3.1 under the work of Beringer et al. (2012) to take various atomic nnumbers from various experiments.

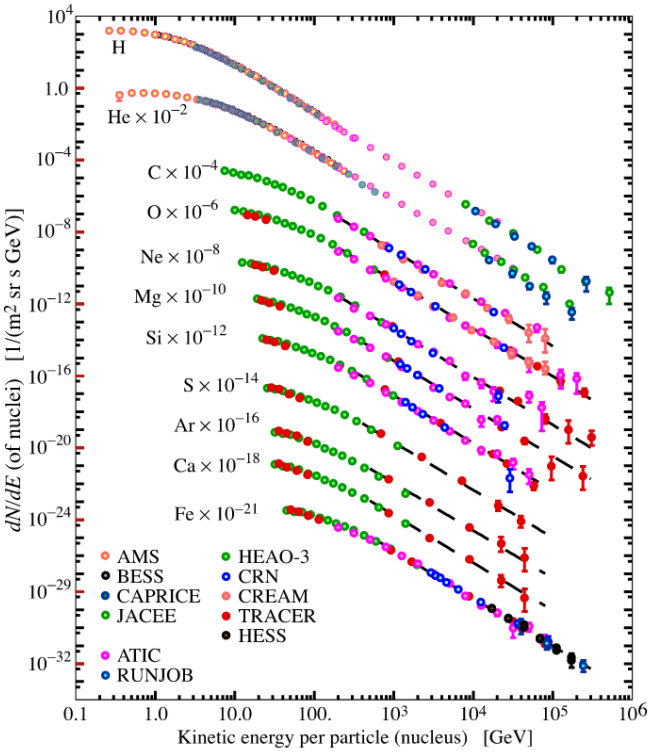

Figure 3.1: Cosmic-ray elemental spectra from various experiments (Beringer et al. (2012))

Since there is a moving plasma inside the Earth, the magnetic field has been generated from the dynamics of the moving charged ions in the plasma. The magnetic field of the Earth has a north pole at the geometric south pole of the Earth and vice versa. The Earth's magnetic field play an important role in the arrival of CR particles because the Lorentzian forces will bend the direction of a moving charged particle depends on the rigidity of the particle. This means the magnetic field line mantles the Earth with a certain direction towards the geometric north pole.

Firstly, it creates the CR cutoff rigidity on the terrestrial where each location of the Earth requires a minimum rigidity of incident charged particles as a condition for arrival. The Figure 3.2 shows a cutoff rigidity on the Earth's surface.

Secondly, incoming charged CRs with a charge has been dragged by

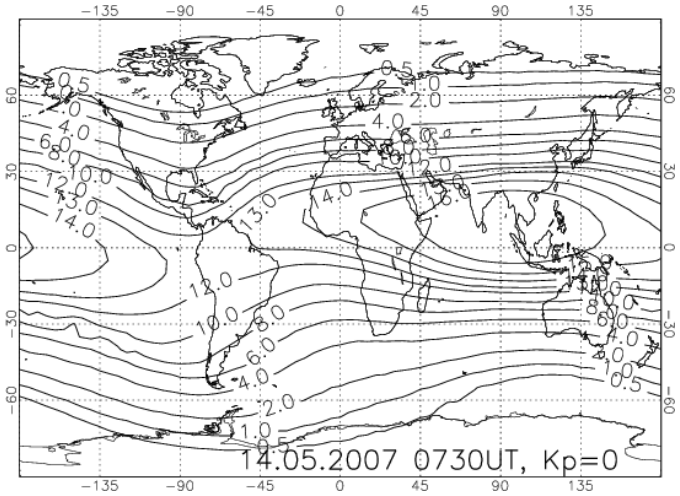

Figure 3.2: World map with computed geomagnetic vertical cutoff rigidity contour lines on a given date (B. et al. (2007))

the Earth's magnetic. Then a charged particle would move as a curve or a spiral depends on the rigidity of an incoming particle which leads to the East-West effects when an orbiting detector could find more particle on the Westside more than on the East side for a significant level of intensity. A pioneer Earth's γ-ray experiment is conducted by Kraushaar et al. (1965) where the detector was deployed on the Explorer XI satellite and orbiting in the sky.

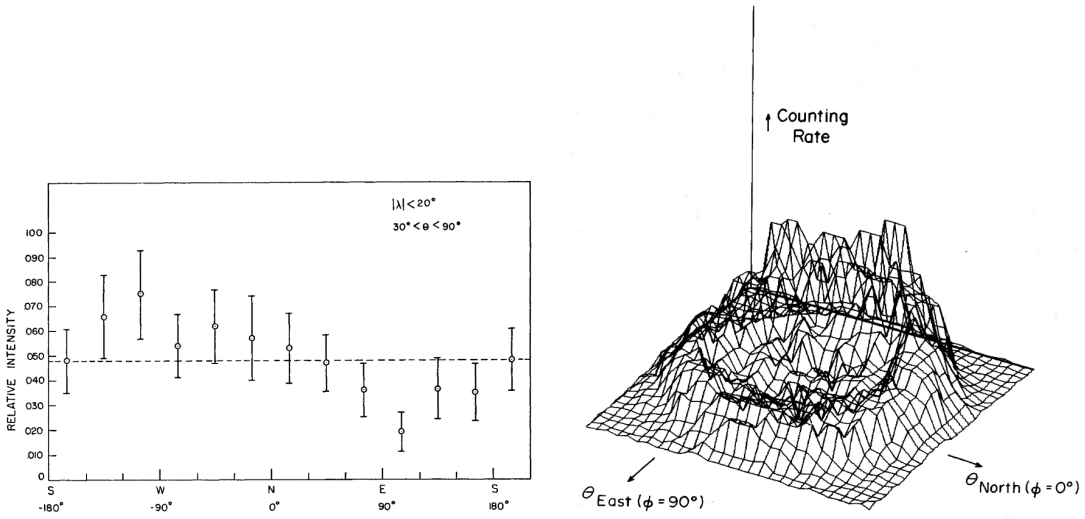

(a) Explorer XI (Kraushaar et al. (1965)) (b) OSO-3 (Kraushaar et al. (1972))

Figure 3.3: The asymmetry of γ-rays East-West intensity

The incoming photon from the East and West direction is the crucial

evidence of the bending of CRs trajectory by Earth's magnetosphere. The first analysis shows a distinguishable intensity from East to West as visualized in Figure 3.3a. The second experiment where the γ-ray detector is attached on Third Orbiting Solar Observatory (OSO-3) and collecting the γ-ray in MeV range. The 2-D plot of the intensity is shown in Figure 3.3b.

Moreover, An early analysis found that the observing γ-rays intensity along the zenith angle from different geomagnetic latitude (λ) is differentiable as shown in Figure 3.4. The reason behind this outcome came from the Earth's rigidity where the incoming particles near the equatorial have less chance to arrive than the north pole and likely to interact with the atmospheric molecules and emits the γ-rays. This is the secondary evidence of how geomagnetic fields play an important role on the trajectory of the CR particles.

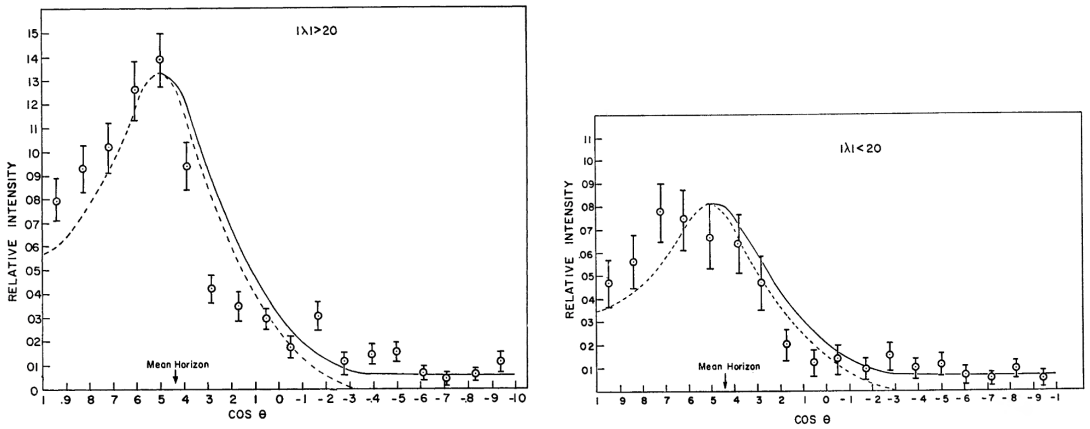

(a) observing above 20°geomagnetic latitude (b) observing below 20°geomagnetic latitude

Figure 3.4: γ-ray intensity along the zenith angle (Kraushaar et al. (1965))

The following experiment of Earth's albedo observations is conducted by sending a second small astronomy satellite (SAS-2) with a higher resolution in angle and observing above 35 MeV up to GeV range (Thompson et al. (1981)). The projected 3-D representation of intensity is shown in Figure 3.5a. A few decades later, another precise $\gamma - ray$ detector has been attached in the CGRO satellite (Petry (2005)). An outcome from the analysis illustrated the bright region around the Earth's limb region as in Figure 3.5b.

The previous details are full of so much experimental evidence. However, Morris (1984) put the weights on the assumption of bright region as seen as albedo

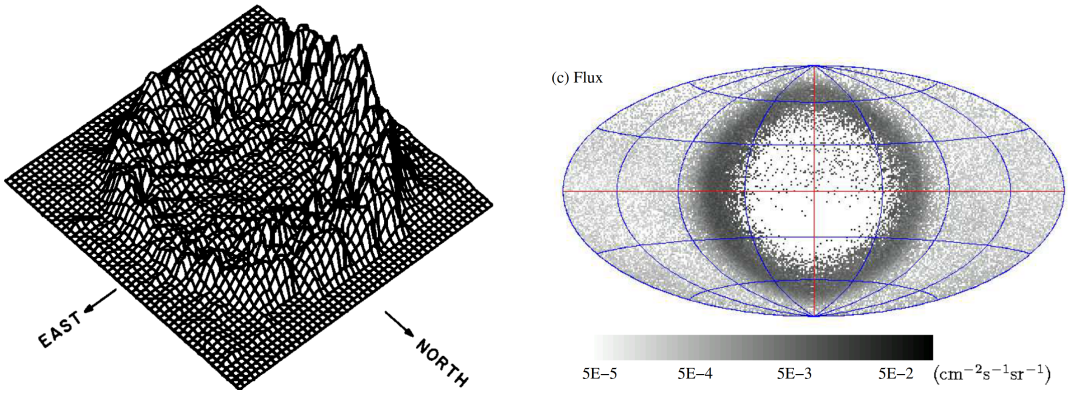

(a) SAS-2 experiment (Thompson et al. (1981)) (b) EGRET experiment (Petry (2005))

Figure 3.5: The Earth's centered intensity plot from the satellite based observations

in γ-ray came from the interaction of proton and the atmospheric nuclei. The study shows the γ-rays intensity and the variation of air depth by differing the zenith angle along limb region as plotted in Figure 3.6 and Thompson et al. (1981) data has been exploited in the analysis.

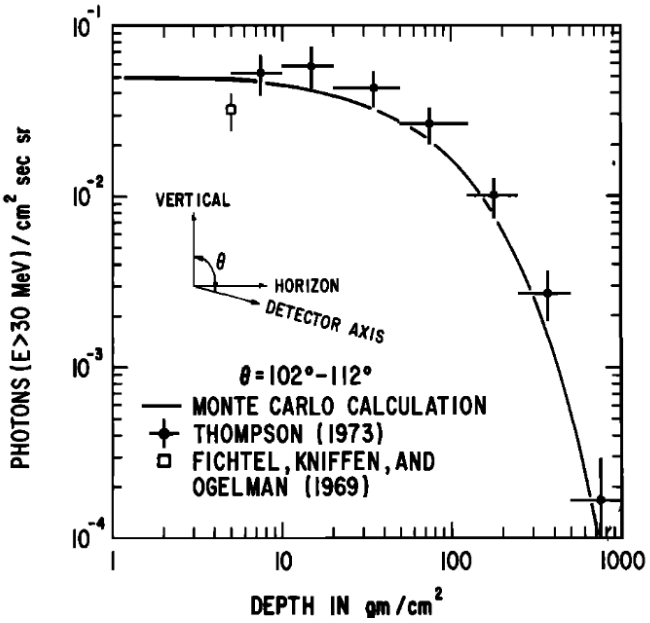

Figure 3.6: Calculated γ-ray intensity with the variation of zenithal angle (Morris (1984))

Furthermore, this study computes the γ-ray spectrum from the bright region as seen as albedo from the Earth's limb and lunar albedo. The Figure 3.7 shows the spectrum from the theoretical calculation. Figure 3.7a identify

the 2 bounds of the limb's region with an approximated air depth. Appealingly, another evidence of the solar activity could cause lower arrival CR particles since the propagating magnetic field drag a charged particle towards outer space. The distinguishable spectrum from this phenomenon is demonstrated in Figure 3.7b.

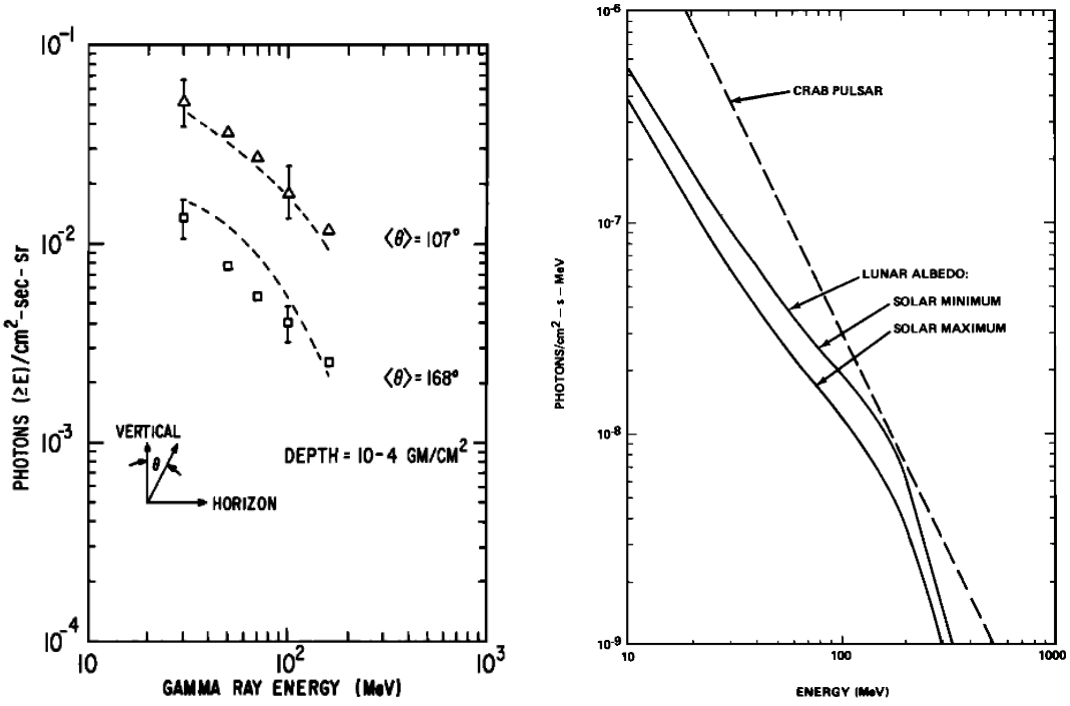

(a) Earth's limb γ-ray spectrum (b) Lunar's atmospheric γ-ray spectrum

Figure 3.7: γ-ray spectrum from proton-nuclei interactions (Morris (1984))

Not so long after *Fermi*-LAT was launched in the sky. In 2009, an early examination of the induced γ-ray emission was observed by the most precise γ-ray detector Abdo et al. (2009). Since there is a huge improvement in the technological side which makes LAT capable of detecting high energy γ-ray from MeV up to TeV. Another discovery from this study was the East-West effect is highly depends on the energy where it was converted from the incident energy of CR particles. The higher energy means the higher rigidity and it would reflect how hard the magnetic field could bend the trajectory. The intensity was divided into 4 energy ranges from a few GeV to a higher GeV that could be considered as the relativistic scheme where the kinetic energy is much higher than the mass as shown in Figure 3.8.

The objective of this work is to indirectly measure the proton spectrum

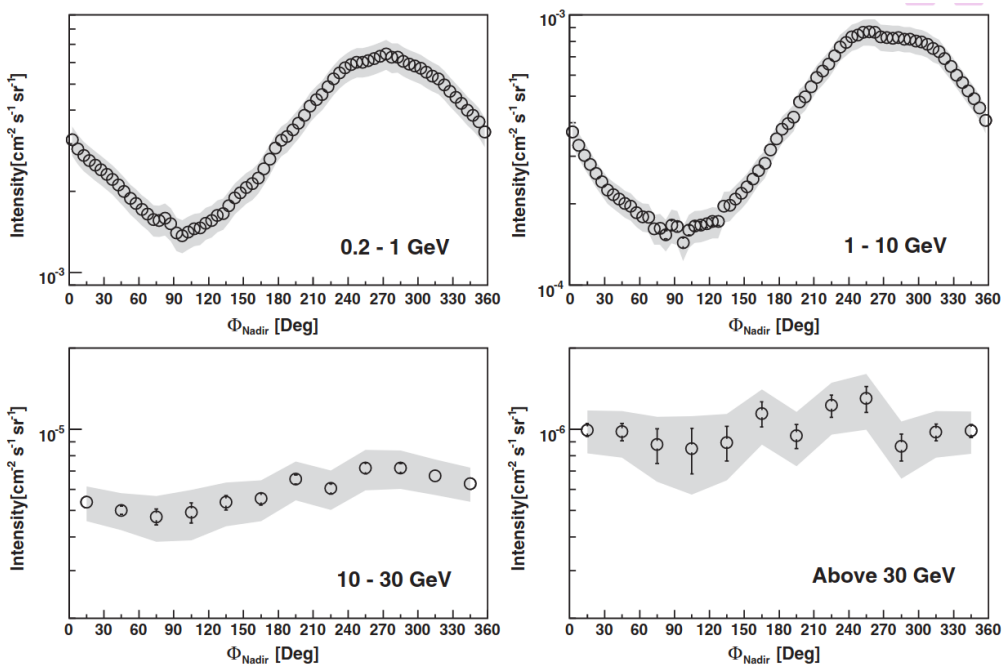

Figure 3.8: γ-rays intensity from limb emission in 4 energy ranges (Abdo et al. (2009))

in GeV range. The direct measurement in an early study of high energy CR particles such as proton and helium were observed by Haino et al. (2004). Another following experiment is Adriani et al. (2011). Both of them still lack the capability to detect such high energy on a scale of a hundred GeV. Nevertheless, there is a clue about the breaking energy in the proton spectrum with very low statistics and leaves room for further study.

Since there is just a clue from the previous direct observations. The indirect measurement of CR proton spectrum has been performed in energy between 90 GeV to 6 TeV by taking advantage of the brightness of Earth's limb from the collision of incident CR protons (Ackermann et al. (2014)). The 5 years of γ-ray data have been exploited by investigating the incident proton spectrum via proton-proton collision model for finding whether CR protons have a breaking point of slope in the power law spectrum. The study found that there is a breaking spectral index in the proton spectrum above 200 GeV Nonetheless, Statistical analysis turns out that it is 1σ significant level.

Back in 2011, one of the most efficient space-based CR detectors was

launched by the carriage of Endeavor space shuttle. The detector has been attached to the international space station (ISS). The main mission of AMS-02 is to search an antimatter, dark matter from measuring CRs. It can detect antimatter such as position and antiproton. This detector is also able to detect other heavyweight nuclei like B, CNO, Ne, etc. In 2015, a proton spectrum has been directly reported and found the breaking at 340 GV (Aguilar et al. (2015)) with very high statistics. Not only the proton but the helium spectrum is also measured and reported in Aguilar et al. (2015).

According to the previous study (Ackermann et al. (2014)), low statistical significant potentially came from lack of the dataset or the methodology from the consequence of indirect measurement. In this work, a similar study will be performed with a larger data size from $\sim$ 9 years of observation. Hopefully, the study could answer the first mentioned clue and put the weights on previous work. Moreover, an improvement of the optimization process by employing the heuristic optimization as well as the high performance calculation of the exposure map for a lesser computational time in γ-ray spectrum calculation.

CHAPTER IV
METHODOLOGY

The procedure of getting data to perform an analysis from the collected data is very important. In order to get a precise Earth's limb γ-ray spectrum to trace back the incident proton spectrum, it is crucial to carefully determine the selection criteria from raw data in many angles base on the objectives. This chapter will begin by giving information on γ-ray flux extraction by providing information on data filtering and the extracting process from scratch. Secondly, the hadronic collision model that forwardly yields the γ-ray spectrum will be discussed and tracing the incident CR's proton spectrum algorithm from heuristic optimization. Lastly, the last sub-chapter contains details of statistical analysis.

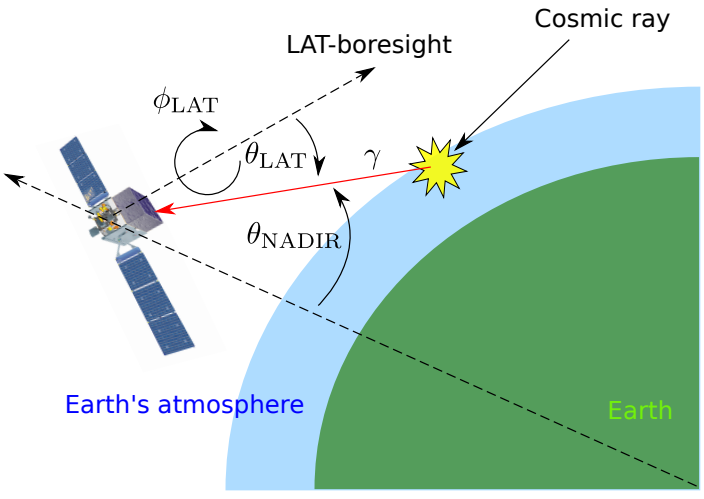

Figure 4.1: Schematics of γ-ray production

The required fundamental concept of spacecraft orientation and the observations of Earth's limb γ emission is another crucial concept. The Figure 4.1 demonstrates the important axis which is θ_{NADIR} represent the angle of how further

from Earth's center in the spacecraft point of view as well as $\theta_{\rm LAT}$ to the angle from incident γ-ray to the detector normal in the domain between 0 to 90°and $\phi_{\rm LAT}$ as the clockwise angle from 0 to 2π.

4.1 Data selection

In this work, 9 years of LAT's flight data has been used to analyze reconstructed photon and their metadata of spacecraft log recorded in a similar format periodically every half minutes. The reconstructed algorithm version is the latest version which is Pass 8 with the cleanest photon events that exist from *Fermi*-LAT data catalogs called ULTRACLEANVETO. To be more precise, the photon data is collected from publically available raw FITs file from the

Only high energy limb photon will be selected from 10 GeV up to 1 TeV. It makes the traceback analysis for gaining the information of CR proton spectrum in rigidity between 60 GV to 2 TV. The definition of γ-ray's limb region is obtained from Abdo et al. (2009) in a given nadir angle from 68.4°to 70.0°. The maximum of incident angle ($\theta_{\rm LAT}$) that was measured from the z-axis of the LAT's foresight is 70°.

4.2 Flux extraction

There are multiple steps from trivial to the complex calculation to obtain the differential flux. The definition when saying flux is a differential flux that is calculated one chunk of energy range at a time as Equation 4.1.

$$\textbf{Flux} \equiv \frac{dN_\gamma}{dE} = \frac{\int_{\text{Limb region}}(\text{Count map/Exposure map})}{\Delta\Omega\Delta E}. \tag{4.1}$$

Since the CR spectrum follows a power law as the exponential form $dN/dR \propto R^\gamma$ as mentioned in the background section. Then the log-log relation of the flux versus rigidity would behave like a trivial linear trend in the plot. Not only the rigidity but in the high energy CR like 10 GeV also makes the energy of the particle almost

the same as the rigidity does. Consequently, the γ-ray spectrum is equally divided in the energy space in the log scale for 50 bins.

To get the spectrum, it is obvious to construct the histogram with 50 bins in a given energy scale as explained in the previous paragraph. The flux of each bin could be computed separately by initializing the empty count map and the exposure map where it represents the exposure time and the effectiveness of the spacecraft when looking at each angle in the sky. Let regards the following example for a deeper understanding. The ideal scenario is when incident γ-ray walk pass through the LAT in a normal line of the detector. The performance would be the highest it could do. On the other hand, if the incident γ-ray arrives with high tile angle from the LAT's plane (High θ_{LAT}). An angle resolution is selected to be 2°in ϕ_{NADIR} and 0.1°in θ_{NADIR}. The reason behind these number is simply from the toy experiment of plotting the result in the 2D histogram and it is selected to be the one as the bin value is not too noisy. In another word, it should not be too small so that the result is not too noisy and it is should not so big due to the limb region could not be seen clearly which leads to the matched photon mixed up with the Earth's γ-rays and collecting too many primaries CR photon.

Basically, the procedure is summarized in these following steps.

1. Make 2D histograms with 25 bins per decade of energy
2. Select photon data and fill in the 2D histograms
3. Calculate exposure maps which include the effective area and livetime of the LAT as it observed the Earth
4. Compute the flux by applying Equation 4.1 in for bin
5. Taking consider background subtraction from a average uniform background photon distribution by treating bin by bin

4.2.1 Exposure map gathering

In fact, step 3 is the most complicated stage in this work. Practically, *Fermi*-LAT was designed for observing the space which makes the spacecraft

logging in equatorial coordinates, not for the Earth's polar coordinates. The LAT position is recorded in equatorial coordinates as well as the LAT's boresight of the detector plane to log their orientation during the orbit. At the end of the day, the coordinates transformation would be performed from multiple frame of reference to LAT boresight for acquiring the exposure of LAT's FoV and reference the effectiveness from LAT's boresight angle dependency. The following content is the full detail of how things going on under the hood.

Coordinate Transformations

Firstly, the spacecraft orbit is recorded in the equatorial coordinate which in a spherical point of view. Defining the cartesian coordinate that share the origin between the celestial point of view and the spacecraft by letting one axis point to the spacecraft could assist the calculation more conveniently as the Figure 4.2. Please note that the x-axis in the equatorial coordinate is called "Equinox".

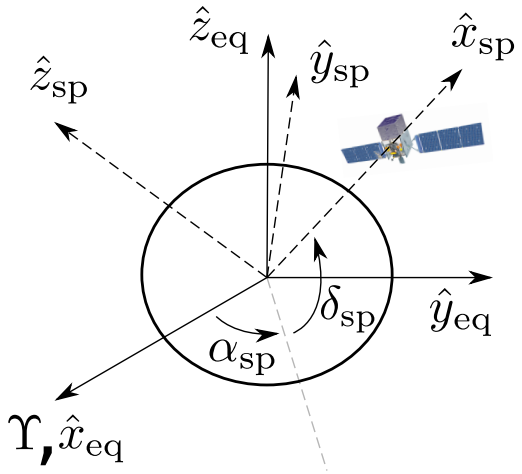

Figure 4.2: Coordinate transform between celestial and spacecraft

However, mapping into the cartesian coordinate by adopting a unit vector in 3 dimensions has been written as Equation 4.2 and the synbolic transformation is represented in Equation 4.3.

$$\begin{aligned}
\hat{x}_{\mathrm{sp}} &= \cos\delta_{\mathrm{sp}}\cos\alpha_{\mathrm{sp}}\hat{x}_{\mathrm{eq}} + \cos\delta_{\mathrm{sp}}\sin\alpha_{\mathrm{sp}}\hat{y}_{\mathrm{eq}} + \sin\delta_{\mathrm{sp}}\hat{z}_{\mathrm{eq}} \\
\hat{z}_{\mathrm{sp}} &= -\sin\delta_{\mathrm{sp}}\cos\alpha_{\mathrm{sp}}\hat{x}_{\mathrm{eq}} + \sin\delta_{\mathrm{sp}}\sin\alpha_{\mathrm{sp}}\hat{y}_{\mathrm{eq}} + \cos\delta_{\mathrm{sp}}\hat{z}_{\mathrm{eq}} \\
\hat{y}_{\mathrm{sp}} &= \hat{z}_{\mathrm{sp}} \times \hat{x}_{\mathrm{sp}}
\end{aligned} \tag{4.2}$$

$$\hat{r}_{\mathrm{sp}} \equiv T_{\mathrm{eq}\to\mathrm{sp}}(\delta_{\mathrm{sp}}, \alpha_{\mathrm{sp}})\hat{r}_{\mathrm{eq}} \tag{4.3}$$

The transformation matrix $T_{\mathrm{eq}\to\mathrm{sp}}$ has been implemented as a matrix in practical analysis due to the convenience for calculation and the compaction in the programming point of view.

Secondly, LAT's boresight coordinates are also referenced in equatorial coordinates. Figure 4.3 demonstrates the relation between an incident plane of the detector on equatorial coordinate and the nadir angle regarding the exposure from LAT to Earth.

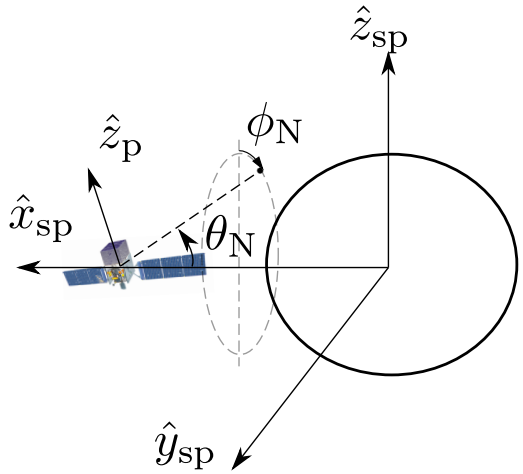

Figure 4.3: Coordinate transform between spacecraft and nadir angle

Unquestionably, it has to be converted into a cartesian point of view to do a mathematical operation for simplicity. A full representation of the coordinates could be written as Equation 4.4 and the compact form is in the Equation 4.5.

$$\begin{aligned}
\hat{x}_{\mathrm{p}} &= \cos\delta_{\mathrm{p}}^{\mathrm{x}}\cos\alpha_{\mathrm{p}}^{\mathrm{x}}\hat{x}_{\mathrm{eq}} + \cos\delta_{\mathrm{p}}^{\mathrm{x}}\sin\alpha_{\mathrm{p}}^{\mathrm{x}}\hat{y}_{\mathrm{eq}} + \sin\delta_{\mathrm{sp}}^{\mathrm{x}}\hat{z}_{\mathrm{eq}} \\
\hat{z}_{\mathrm{p}} &= \cos\delta_{\mathrm{p}}^{\mathrm{z}}\cos\alpha_{\mathrm{p}}^{\mathrm{z}}\hat{x}_{\mathrm{eq}} + \cos\delta_{\mathrm{p}}^{\mathrm{z}}\sin\alpha_{\mathrm{p}}^{\mathrm{z}}\hat{y}_{\mathrm{eq}} + \sin\delta_{\mathrm{sp}}^{\mathrm{z}}\hat{z}_{\mathrm{eq}} \\
\hat{y}_{\mathrm{p}} &= \hat{z}_{\mathrm{p}} \times \hat{x}_{\mathrm{p}}
\end{aligned} \tag{4.4}$$

$$\hat{r}_{\mathrm{p}} \equiv T_{\mathrm{eq}\to\mathrm{p}}(\delta_{\mathrm{p}}^{\mathrm{x}}, \alpha_{\mathrm{p}}^{\mathrm{x}}, \delta_{\mathrm{p}}^{\mathrm{z}}, \alpha_{\mathrm{p}}^{\mathrm{z}})\hat{r}_{\mathrm{eq}} \tag{4.5}$$

Similarly, $T_{\mathrm{eq}\to\mathrm{p}}$ is also considered as a transformation matrix in the computation for monotizing the source code as well as keeping consistency in the logic.

Again, all those representations just for mapping the LAT's boresight coordinate to link with the nadir coordinate to accumulate the exposure from the spacecraft's FoV. The spacecraft coordinate can be written as a dependency of Earth's polar coordinate as Equation 4.6 in the cartesian system.

$$\hat{r}_{\mathrm{sp}}^{\mathrm{o}}(\theta_{\mathrm{N}}, \phi_{\mathrm{N}}) \equiv -\cos\theta_{\mathrm{N}}\hat{x}_{\mathrm{sp}} + \sin\theta_{\mathrm{N}}\cos\phi_{\mathrm{N}}\hat{z}_{\mathrm{sp}} + \sin\theta_{\mathrm{N}}\sin\phi_{\mathrm{N}}\hat{y}_{\mathrm{sp}} \tag{4.6}$$

By the end of the day, extracting the relations to simplify the LAT's boresight coordinate could be contained by one inversion of transformation matrix from equatorial to spacecraft and transform it to plane of the detector as written in the compact form in the Equation 4.7.

$$\hat{r}_{\mathrm{p}}^{\mathrm{o}}(\theta_{\mathrm{N}}, \phi_{\mathrm{N}}) = T_{\mathrm{eq}\to\mathrm{p}}(\delta_{\mathrm{p}}^{\mathrm{x}}, \alpha_{\mathrm{p}}^{\mathrm{x}}, \delta_{\mathrm{p}}^{\mathrm{z}}, \alpha_{\mathrm{p}}^{\mathrm{z}})\left[T_{\mathrm{eq}\to\mathrm{sp}}(\delta_{\mathrm{sp}}, \alpha_{\mathrm{sp}})\right]^{-1}\hat{r}_{\mathrm{sp}}^{\mathrm{o}}(\theta_{\mathrm{N}}, \phi_{\mathrm{N}}) \tag{4.7}$$

Geometrically, an angular coordinate of the LAT plane could be obtained from a normalized component of the cartesian unit vector as in Figure 4.4. The exposure accumulation has been calculated in every single grid from the previous relation.

Parallel Computations

From the previous section, it is obvious that the complexity of the code becoming large due to the transformation operation. For example, a plain matrix

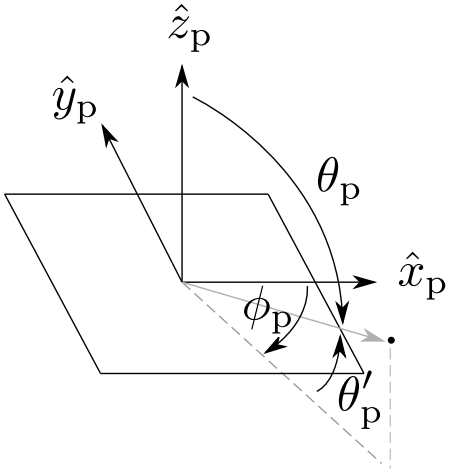

Figure 4.4: Detector's boresight in cartesian and polar coordinate

inversion cost $\mathcal{O}(n^3)$ where n is 3 because it is a 3 by 3 matrix in this case. Not only the inversion, but the matrix multiplication also cost the same amount of complexity which causes a long run in the execution time because the original program has been designed in sequential execution.

Nevertheless, the spacecraft log file namely "FT2" has been recorded row by row which equivalently to a CSV format as a plain table with the specific columns. Since the objectives are to determine the exposure map by counting the exposure time as well as the effectiveness of the spacecraft from each angle for a given small range of energy which means that the energy could be approximate as one energy for getting the effective area in each angle of the LAT during calculation. Moreover, the exposure could be calculated parallelly for each step or in each row of the FT2 due to the property of the exposure map. Consequently, splitting the exposure map and calculate parallelly is possible to get rid of the performance issue.

The code is implemented in Message Passing Interface (MPI). The framework provides a simple protocol without knowing any type of protocol or zero required network knowledge. It assists the user to freely control multiple processes with full control of each process. According to Flynn's taxonomy of computation, this work exploits the Multiple Instruction Multiple Data (MIMD) architecture to utilizing the resources in a distributed systems.

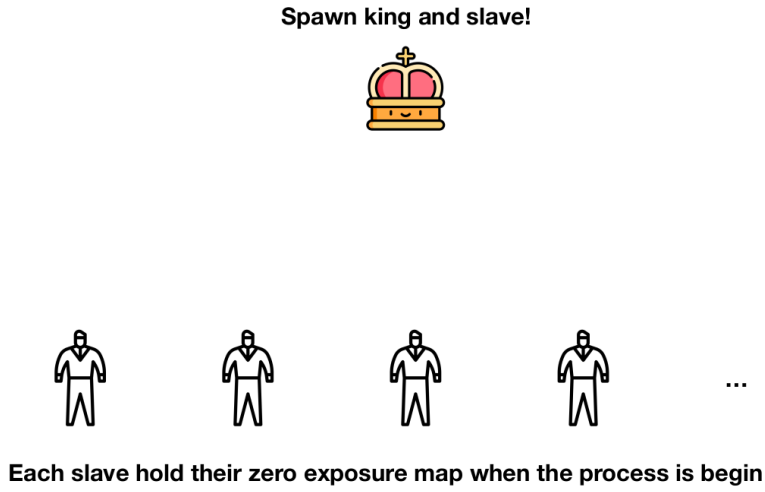

Figure 4.5: Spawning the king and slave processes

To begin with, the calculation, initializing the exposure map with a separate workers and send multiple rows to the workers in the same amount is trivial and waste a lot of resources since there will be a fast worker who do a calculation fast and the slow worker due to the cluster is composed of non-monolithic nodes with different performances. The trivial calculation will lock the resource in the cluster and blocks the other researcher who wants to run because of the resource allocation issue. To maximize the usage of the CPU-based cluster computing, there is a mechanism called the "Master-Slave technique". The algorithm has been designed for utilizing the resource by spawning a king as the process manager and multiple slaves to be a process worker. The starting process could be demonstrated in Figure 4.5.

After that, the FT2 rows will be sent to slaves sequentially until all workers hold a small chunk of data and do their jobs. In practice, there is metadata attach to the message. One of the options is the status tag. The status tag sends to the worker to declare the state of the process whether it is in the calculation or the finishing. Figure 4.7 illustrates the non-sequential sending of the workload. The idea is simply sending a small task to an available worker and skip a busy worker without disturbing them. This mechanism allows the execution to utilize the resource in the cluster without wasting in the free worker.

By the end of the day, if the task is completely sent. The master process

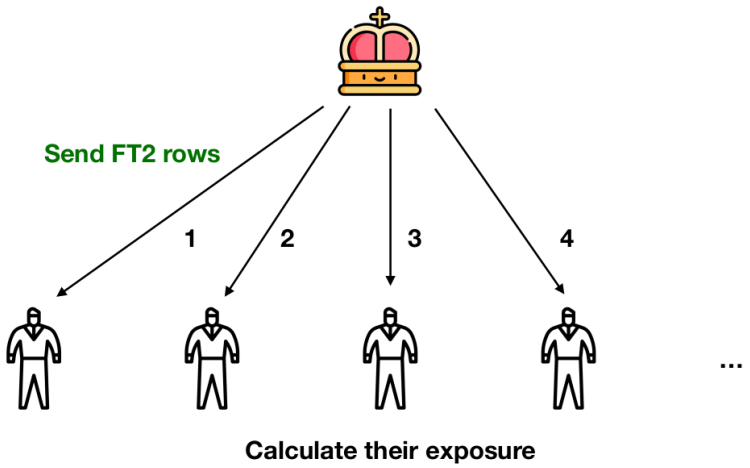

Figure 4.6: Master process send a small task to workers

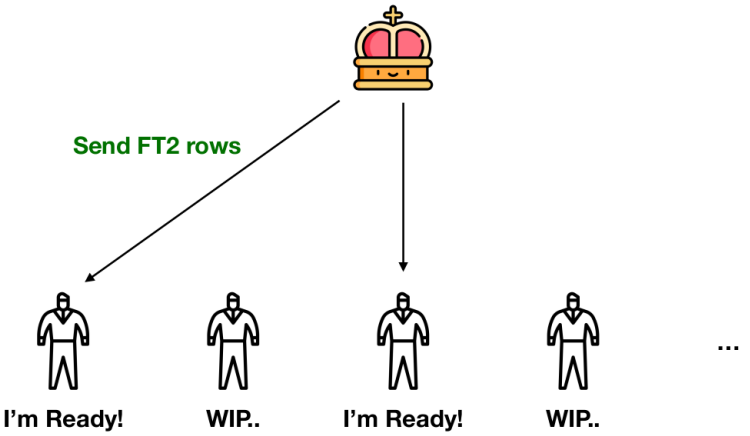

Figure 4.7: Aynchronous sending to an available worker

will send the status tag as done to be an announcement of the finishing period. Then the exposure map of each worker will be gathered in the master process for superposition and dump it to unify an exposure map. In addition, the calculation in an early period of testing is reported in Appendix A.

4.3 Hadronic Collision Model

The proton spectrum power law in rigidity is described in Equation 4.8 as a single power law (SPL) where the γ represents the spectral index of the

model. In fact, the spectrum has been observed as the differential flux in energy. Converting process between the ridigity spectrum and the energy spectrum is derived in Appendix B to obtain a precise calculation.

Single power law (SPL)

$$\frac{dN}{dR} = R_0 R^{-\gamma} \tag{4.8}$$

The most crucial part of this work is to determine if there is any breaking in the spectral indices in the power law. To represent a single breaking energy, the broken power law (BPL) could be modeled the spectrum in rigidity as Equation 4.9.

Broken power law (BPL)

$$\frac{dN}{dR} = \begin{cases} R_0 R^{-\gamma_1} \ : \ E < E_{\text{Break}} \\ R_0 [R(E_{\text{Break}})]^{\gamma_2 - \gamma_1} R^{-\gamma_2} \ : \ E \geq E_{\text{Break}} \end{cases} \tag{4.9}$$

The scattering process of the hadronic collision from proton hitting the atmospheric molecules. The collision from incoming proton kinetic energy above 10 GeV could be modeled by proton-proton collision with an approximation that depends on the majority of the air components. Model for the collision of proton-proton which yields γ-ray as a secondary product as a distribution in the spectrum has been derived in Equation 4.10 from Kachelrieß & Ostapchenko (2012) work.

$$\frac{dN_\gamma}{dE_\gamma} \propto \int_{E_\gamma}^{E_{\max}} dE' \frac{dN_p}{dE'} \frac{d\sigma^{pp\to\gamma}(E', E_\gamma)}{dE_\gamma} \tag{4.10}$$

Where $d\sigma^{pp\to\gamma}(E', E_\gamma)/dE_\gamma$ contains a scattering amplitude of a given kinetic energy proton and the spectrum of the γ-ray. Atmospheric components mostly consists of nitrogen as the majority and the oxygon (Wallace & Hobbs (2006)). The cross-section from proton-proton collision and proton-nitrogen collision is roughly approximate as the multiplicative relation since there is plateau curve in the energy range in this analysis. The relation of the proton-proton scattering amplitude and the proton-nitrogen is obtained from Atwater & Freier (1986a) where it highly depends on the atomic numbers of the air molecules.

However, the second highest fraction of the arrival CR particles on Earth is an alpha (α) particle. The helium nuclei can interact with the nitrogen and produce high energy γ-rays depends on how much kinetic energy α-particles is holding. Another estimation has been exploited by applying $\sigma_{\alpha N}/\sigma_{pN}$ to be a constant around 1.6 at the energy range in GeV from the same relationship of the proton-air collision model. Hence, derived equation of the scattering process from incoming proton and α-particle with air molecules to produce γ-ray spectrum could be shown as Equation 4.11

$$\frac{dN_\gamma}{dE_\gamma}(E_\gamma) \propto \sum_{E_i'} \left[\frac{E_i'}{E_\gamma}\Delta(\ln E_i')\right]\left[f_{pp}\frac{dN_p}{dE_i'}\left\{1+\frac{\sigma_{\mathrm{HeN}}}{\sigma p\mathrm{N}}\left(\frac{dN_p}{dR}\right)^{-1}\frac{dN_{\mathrm{He}}}{dR}\frac{dR_{\mathrm{He}}}{dR_p}\right\}\right], \tag{4.11}$$

The CR helium spectrum would not be measured in this work since there will be multiple parameters that leads to an overwhelming local optimum. The spectrum of α-particles is directly measured by Aguilar et al. (2015) and fix the distribution as one function rather modeled spectrum of CR proton spectrum. The full detail of the equation derivation will be demonstrated in D.

4.4 Optimization

Determining the best-fit spectral model requires an objectives function to represent how well the model match with an observed data. A proper methodology for fitting or optimization in another word is also a crucial part since it is likely that the local optimum exists in the parameters space. A poor optimization could lead the best-fit stuck in a local minimum and yield a poor result. For better escaping local optima, heuristic optimization is employed for finding the best-fit of the model in parameter space.

Poisson likelihood function

An objective function is defined as Poisson likelihood function in the Equation 4.12. The reason behind the selection of the Poisson function came from

the observed model and measurement is considered as a number of photons in each bin of the histogram. Converting the model spectrum to be a count histogram is simply multiplied by the integral of the exposure map in the limb region.

$$\mathcal{L} = \prod_{i=1}^{N} P_{\text{pois}}(n_{\text{i,model}}, n_{\text{i,measurement}}) \tag{4.12}$$

Since the spectrum order is in different order of magnitude, then a proper way to define an objective function is to redefine a likelihood as a log-likelihood function for numerically convenient like Eq 4.13.

$$Sum = \sum_{i=1}^{N} -\log P_{\text{pois}}(n_{\text{i,model}}, n_{\text{i,measurement}}) \tag{4.13}$$

To sum up, a given proton spectrum yield a distribution of γ-ray spectrum to be converted into a count histogram and comparing with the real measurement. Not only for numerical convenient but the negative sign also makes an algorithm to minimize the system rather than maximize a likelihood.

Particle Swarm Optimization (PSO)

In the early phase of the optimization, a plain gradient descent optimization has been used for model fitting. The result turns out that with different initial parameters, the different best-fit model has changed which implies the local minimum in the problem. Even there is no method to guarantee the global minimum but the heuristic optimization could be a better option for handling this type of problem. One kind of most widely used algorithm is particle swarm optimization (PSO) and it is invented by Kennedy & Eberhart (1995).

In order to get a best fit spectral indices, employing the Particle Swarm Optimization (PSO) by randomly initiate many particles in a given range of the parameter space and find the local and global best fit in each step of the iteration. Then rest of them would slowly move toward to the local and global position in parameter space with a proper weight. The iteration process will stop when the standard deviation of the objective function from every particle less than a decimal. The explicit formula for every iteration k, particle i move with velocity v_k^i is

$$v_{k+1}^i = \omega v_k^i + c^b r_k^b [b_k^i - x_k^i] + c^B r_k^B [B_k^i - x_k^i], \tag{4.14}$$

and updating the particle i with

$$x_{k+1}^i = x_k^i + v_{k+1}^i. \tag{4.15}$$

where

- x_k^i represent variable that particle i hold
- b and B are best local and global parameter sets along the optimization process
- Set $\omega = 0.2$, $c^b = 0.2$ and $c^B = 0.3$

4.5 Statistical significance

Certainly, larger model parameters or complexity would yield a better performance except it is overfitting the problem. The critical issue is to answer how much significance the alternative model could outperform the trivial model. As the language of statistics would consider as two hypotheses. One for null and one for alternative approach.

For this case, BPL has 2 more degrees of freedom (DOF) than SPL. Unquestionably, if there is a good optimization procedure, the objectives function would say BPL is better SPL. As mentioned from the previous paragraph, the significance level has to be taken into account to put the weight on the study. Theoretically, regarding the model likelihood with a given set of parameters could be determined in the general case as Wilk's theorem define the relation in Equation 4.16.

$$\mathcal{L} \equiv \prod_{\alpha=1}^{n} f(x_\alpha, \theta_1, \theta_2, ..., \theta_h) \tag{4.16}$$

where

- x_α is represent a variant from model and data

- θ_i is a degree of freedom (DOF)

The practical usage to compare the null hypothesis and the alternative hypothesis as similar to one-tail hypothesis testing with a given dependency in more DOF has been adopted by Huelsenbeck & Crandall (1997). This method called "Likelihood ratio test (LRT)". The compact formula is shown in Equation 4.17.

$$\mathrm{LRT} = -2\ln\left(\frac{\mathcal{L}_{\mathrm{null}}}{\mathcal{L}_{\mathrm{alternative}}}\right) \tag{4.17}$$

CHAPTER V
RESULTS AND DISCUSSION

The content of this chapter would be reported as the analysis procedure from step one to the end. The first part is the data correction process, count maps from the raw count as well as exposure map from the parallel computation, the spectrum and inversion model fitting by heuristic optimization.

5.1 Limb's angle correction

Theoretically, the peak profile of the θ_{NADIR} would be the same. From the observations, the nadir angle change through time evolving since the spacecraft altitude is gradually getting lower in each year which will affect the LAT point of view when it sees the Earth.

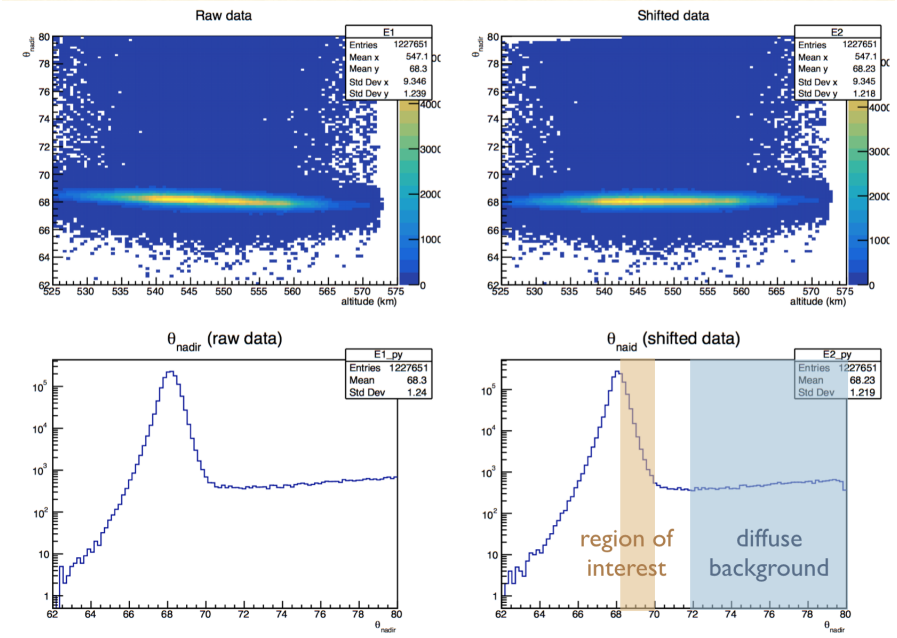

Figure 5.1: Distribution of nadir angle before and after altitude correction

The top-left of Figure 5.1 demonstrates how much spacecraft orbiting

altitude correlate to the θ_{NADIR} by a 2D heatmap plot of photon intensity. The bottom-left histogram came from the projection of the previous raw count 2-D histogram which has a peak around 68°. Both bottom and top right histograms was constructed from exactly the same logic but there is one different variable. The shifted nadir angle has been calculated to reduce the effect from the spacecraft and the region of interest has been highlighted as orange for calculating as the limb spectrum and the blue zone is a diffusive background to be used in the background subtraction.

The brightness of Earth's limb is much brighter than the diffusive background on the map. The region of interest and the background intensity has a huge difference in approximately an order or magnitude.

5.2 γ-ray spectrum measurement

According to the definition from Equation 4.1, the first step is the construction of the count map of the Earth's centered coordinates. Regardless of the photon energy, a week of the accumulated photon has been plotted in the Figure 5.2 to visualize the raw count of the sample data on the count map.

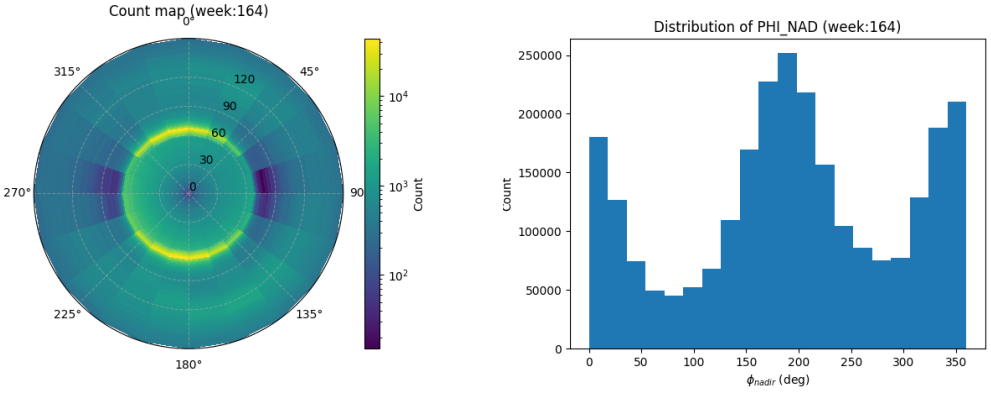

(a) Photon count map (b) Photon distribution along the nadir angle

Figure 5.2: An example distribution of γ-ray from a single week

The limb's region could be easily observed in the bright ring above a dashed line of 60°nadir angle. Figure 5.2 an also shows the brightness of the

southern and northern hemispheres. Further investigating of the East-West effects could be illustrated by projecting the 2-D histogram into 1-D histogram of the nadir angle as in Figure 5.2b. Nevertheless, the explanation of the East-West a rough description and still incomplete since it does not take the exposure into account yet.

Applying criteria from the data selection such as event class, LAT's incident angle would affect the result from the histogram filling. In practice, each histogram was constructed for their belonging bin of the histogram in the energy domain. Hence, the multiple count map will be created for serving their energy ranges as in the Figure 5.3.

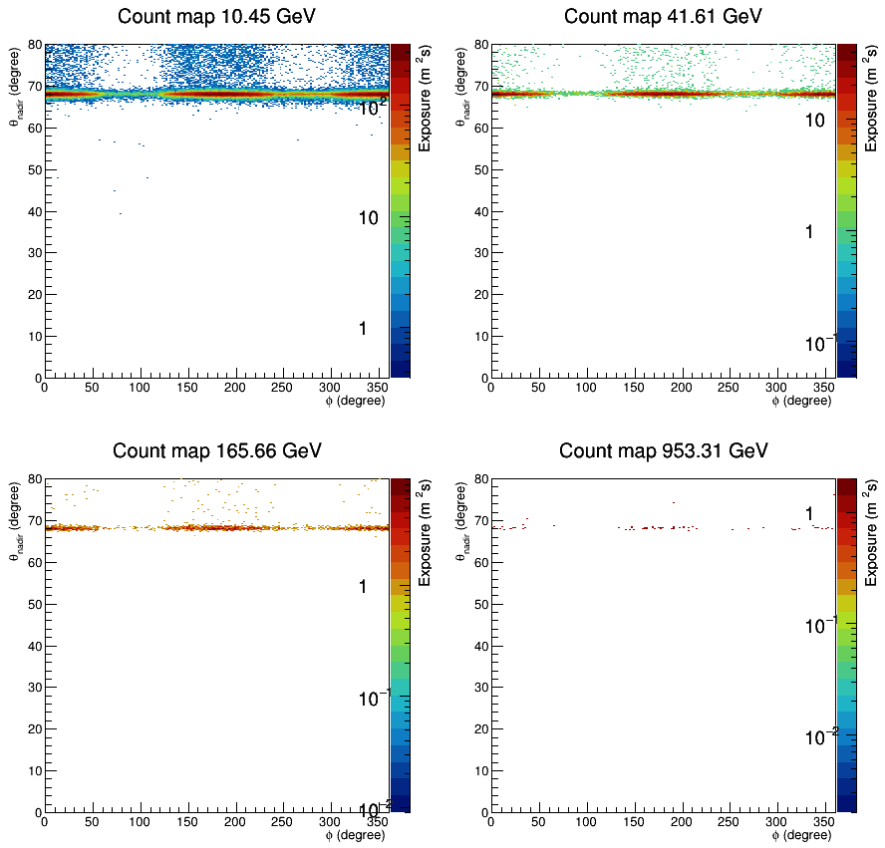

Figure 5.3: Cartesian plot of the photon histograms (title represent mean of the energy range)

However, looking at polar coordinate plotting from the cartesian point of view would not be a proper way. Figure 5.4 is another angle of viewing the same data but in their natural orientations. Both visualizations show that the Earth's

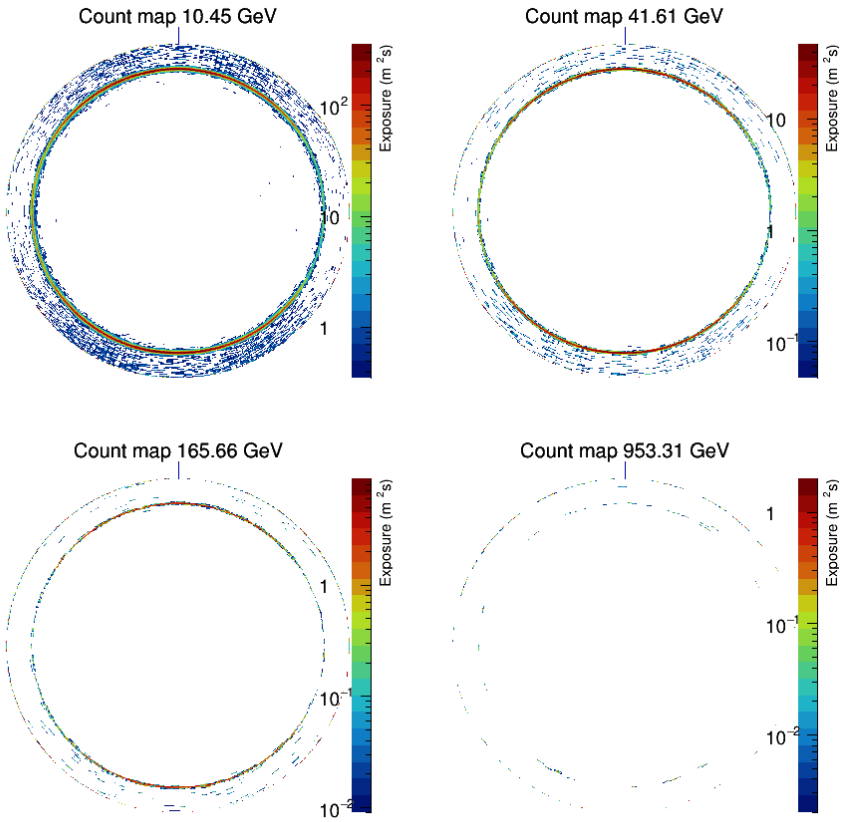

Figure 5.4: Polar plot of the photon histograms

limb region in γ-ray is the shinest band for all interesting energy. It is also obvious to say that the more energy filtering condition, the less photon would match the criteria.

The next step is the exposure calculation. The exposure map is computed by accumulated exposure time from the LAT's FoV and also takes the effectiveness of the detector for correcting an angle dependency. By the end of the day, a unit from the calculation will be an area multiple by the time. The raw cartesian plot is visualized in Figure 5.5 with an attached axis.

The heatmaps show that the exposure intensity in the sky is much higher than the Earth in an order of magnitude because LAT was designed for seeking flare events in the space rather than looking at Earth. Regarding a given nadir angle between 60°to 70 °, the spacecraft seems to look at the northern or southern hemisphere rather than the eastern and the western side. The color of

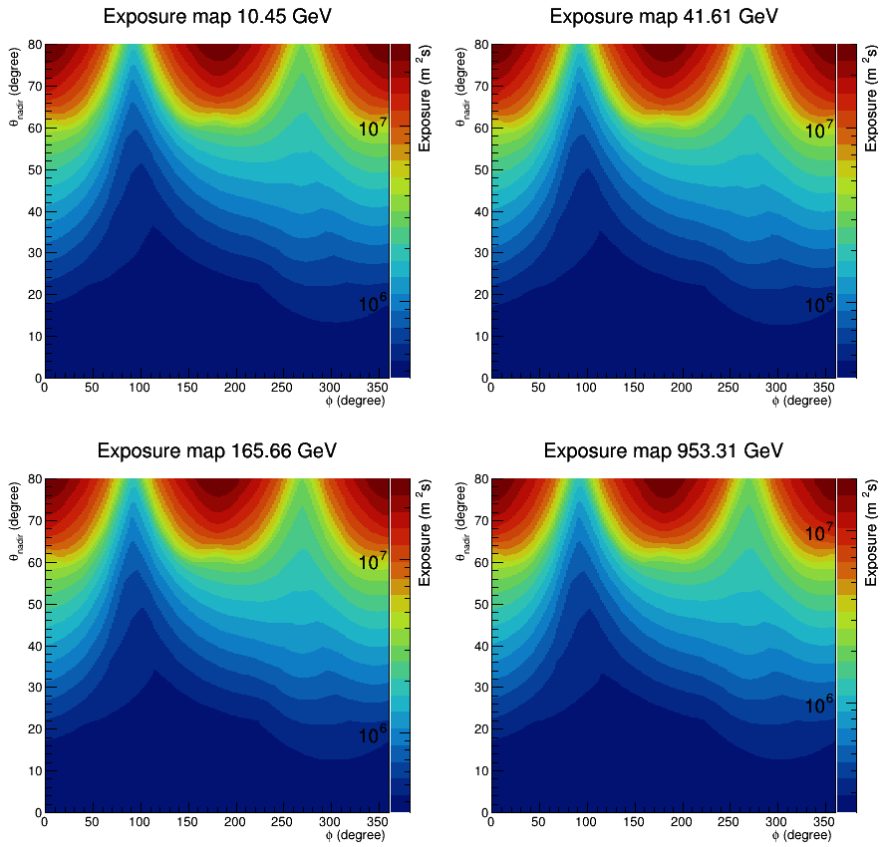

Figure 5.5: Cartesian plot of the exposure histograms

the at 270°(West) is more intense than 90°(East) means that the spacecraft tends to peek in the Westside more than Eastside. The reason might come from the trajectory of the charged particles were bent and produce a γ-ray which potentially could convince LAT to look at them rather than the other side because it has a chance to trigger the GBM. The 2-D histograms in polar coordinates have also been plotted in Figure 5.6.

The last step starts with initiating the new map that was defined by the division from the count maps and the exposure maps. After that, integrating the limb region in the polar coordinates to get a single scalar value. The scalar is then divided by the gap of the energy bin and the solid angle as a unitless quantity. Repeating a given description for all energy bins in the γ-ray spectrum and subtracts by the background would yield the final photon spectrum as in Figure 5.7.

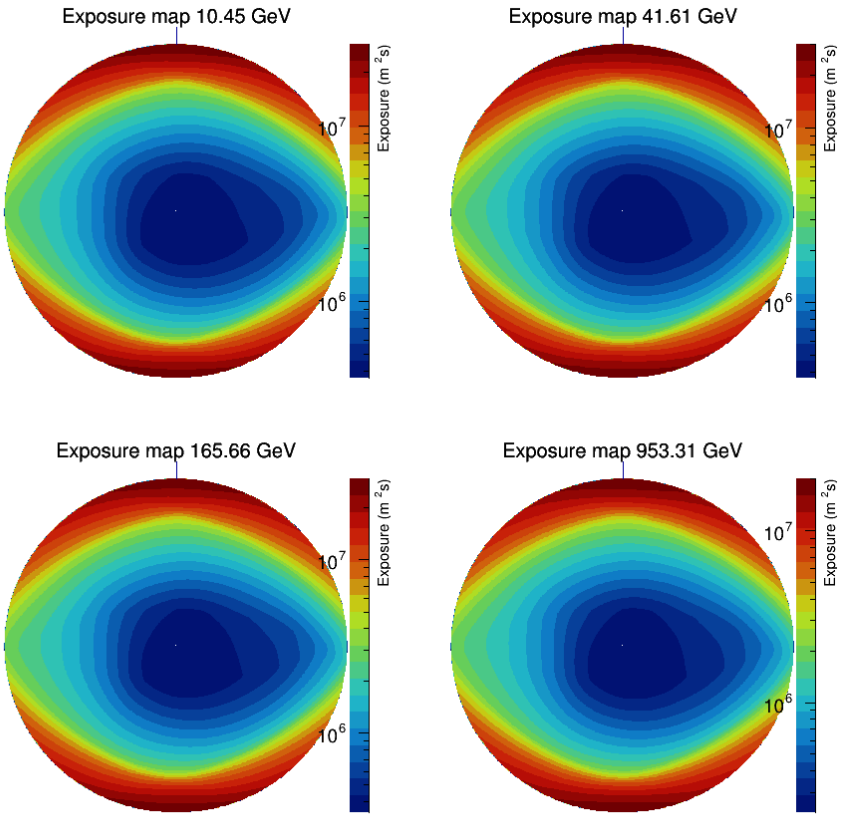

Figure 5.6: Polar plot of the exposure histograms

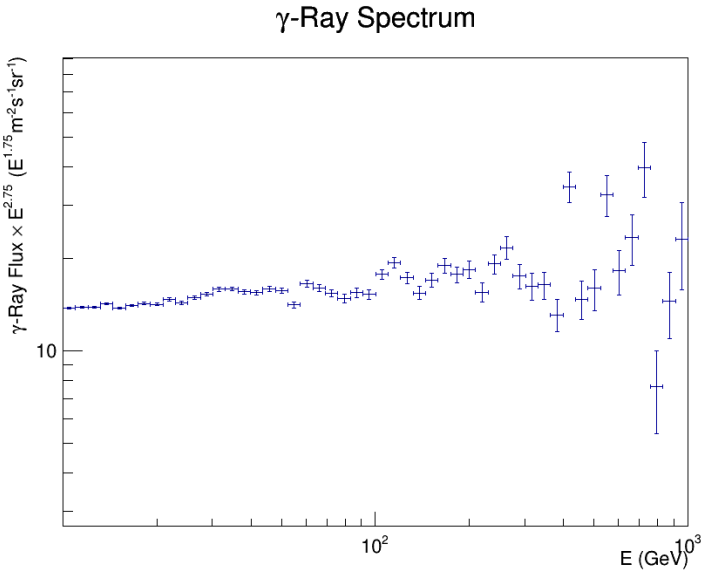

Figure 5.7: Measured γ-ray spectrum

In addition, exploring the γ-ray intensity from the visualization of the Earth's centered coordinates would be informative aspects to observe the variation of the photon intensity along the nadir angle as well as the East-West effect. The cartesian plotted is in Figure 5.8 and the polar form as in the Figure 5.9. Comparing the intensity along the peak of theta nadir in the cartesian plot from the East (ϕ=90°) and West (ϕ=270°) would reflect that the band of the intensity in the west is slightly thicker than in the East and the color of the peak center is more a little darker than the other side. It means that not only the intensity but also the ring thickness of the limb region is larger from West to East.

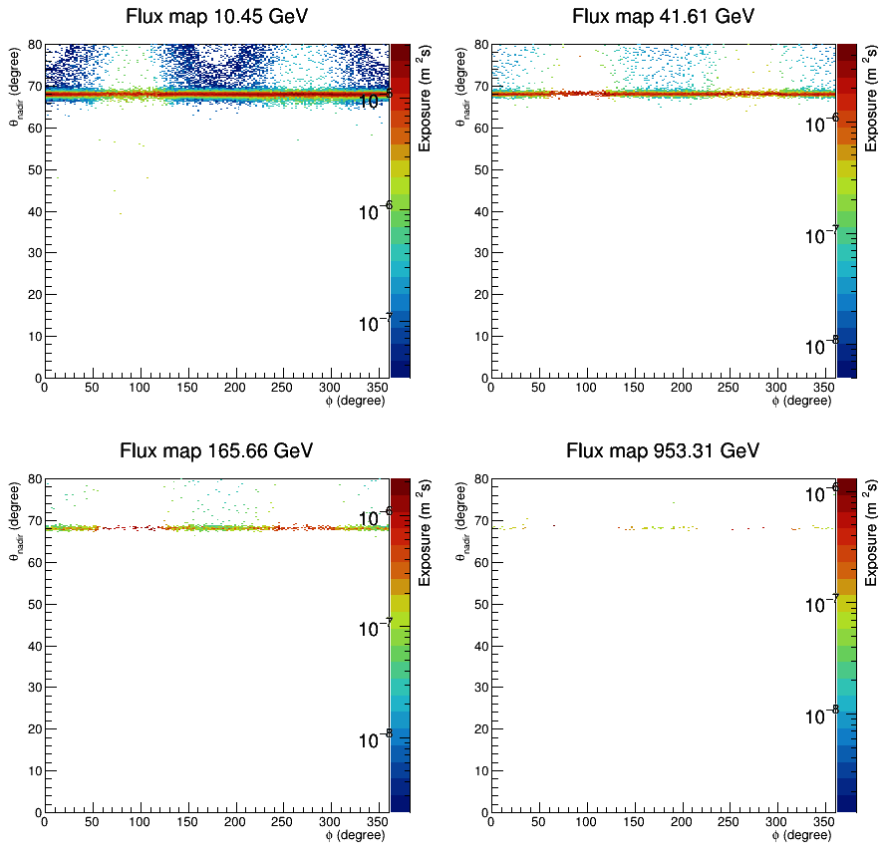

Figure 5.8: Cartesian plot of the flux histograms

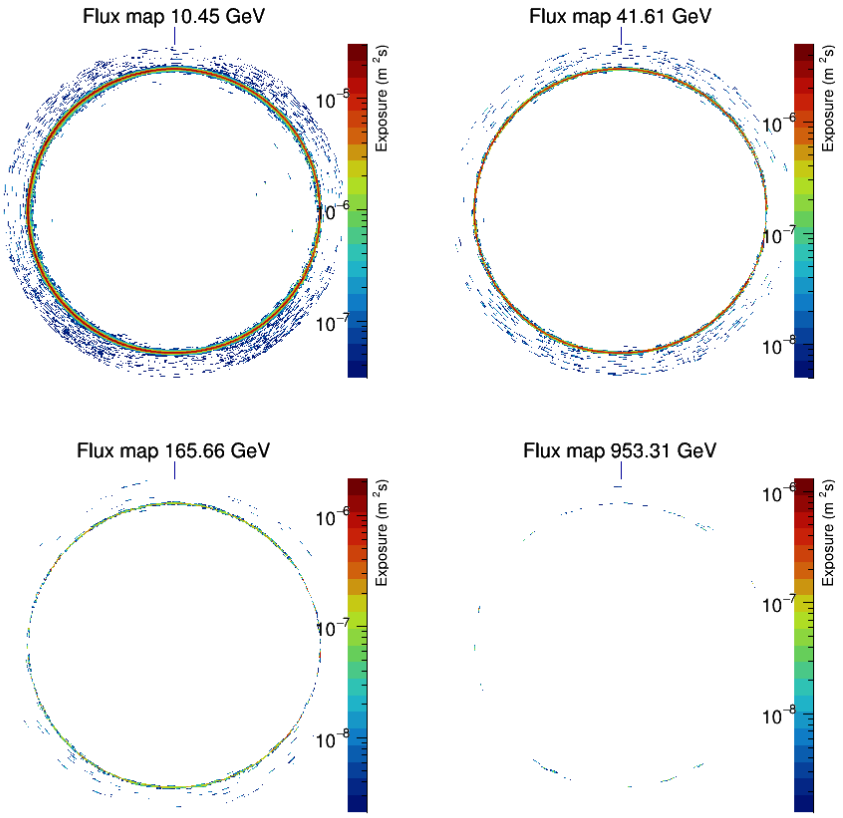

Figure 5.9: Polar plot of the flux histograms

5.3 Best fit result

The optimized parameters for SPL and BPL models are summarized in Table 5.1. Best fit γ-ray from both models are visualized in the Figure 5.10 along with spectrum from the measurement.

Best fits	γ_1	γ_2	E_{Break} (GeV)
SPL	2.70	-	-
BPL	2.86	2.63	333

Table 5.1: Optimization results

The comparative illustration also be visualized in the Figure 5.11 with a scaled spectra from both models to collate two other direct observations of the space-based experiments. It is obvious to see the consistency of BPL with the direct measurements in the bellowing sub-figure is more corresponding than the SPL model in the top sub-figure because the breaking point of the BPL does looks

more likely to be a proper model where the x-axis is the same rigidity scale.

However, a more complex model would perform better than the model that has less degree of freedom in practice. Determining the statistical significant would be the best way to answer whether CR spectrum is naturally described as a BPL indeed. The significant level could be determined by applying the objective function to Equation 4.17 for testing one-tail hypothesis-like from the null hypothesis comparing to an alternative hypothesis which is the model of breaking of spectral indices and non-breaking scheme or SPL versus BPL in another word. The significance is around 1.38σ or at 92%.

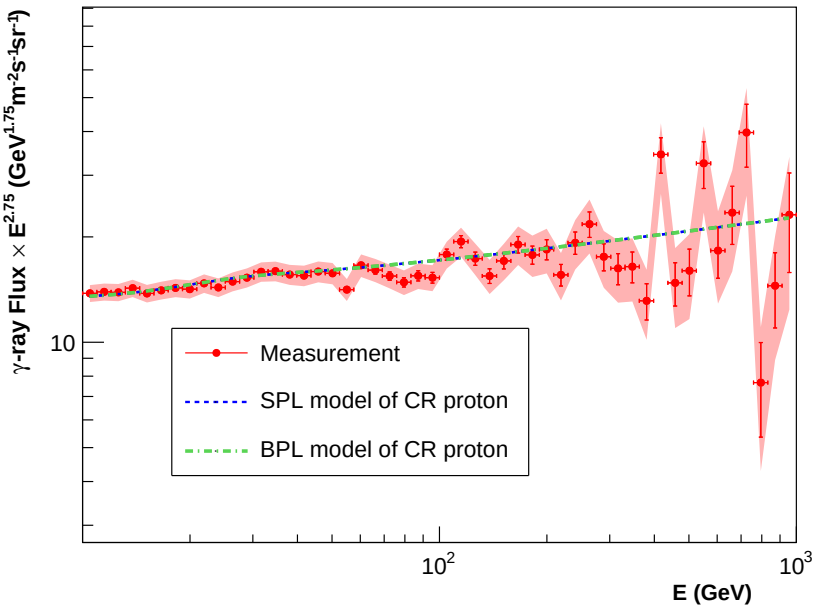

Figure 5.10: The γ-ray spectra calculated from the SPL (red) and BPL (blue) models of CR proton which best fit with the measured Earth's γ-ray spectrum in the thin-target regime (red)

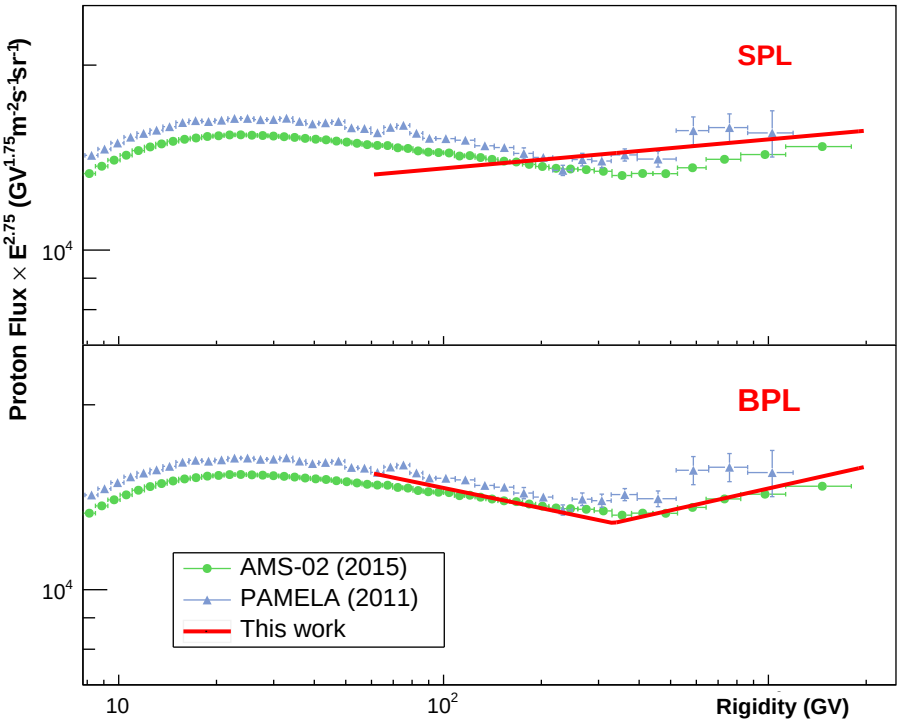

Figure 5.11: Best-fit CR proton spectrum from this work (red) compared to the measurementsby AMS-02 (blue) and PAMELA (green)

CHAPTER VI
CONCLUSION

In this study, the incident CR proton spectrum was tracing by using the limb γ-ray. The measured γ-ray spectrum is constructing by taking the exposure of the LAT and the effective area into account where on the Earth-centered coordinates. The exposure calculation is calculated from the relation of the angle between the LAT's boresight and nadir angle because given nadir angle and the spacecraft orientation affects the performance of the measurement. After that, an indirect measurement of the proton spectrum was inversely computed via the $pp \rightarrow \gamma$ interaction model with a heuristic optimization technique.

Since the *Fermi*-LAT was launched in June 2008. The data has been collected from 7 August 2008 to 16 October 2017. The collection from 9 years of observations was recorded for both γ-rays data and the spacecraft orientation logging. The LAT mostly observing the sky and looking for a flare of γ-rays. However, there is a moment that LAT FoV can see the Earth or even stare at the Earth for some reason. Filtering photon from the Earth's limb region was done by selecting an incoming photon in the direction between 68.4°- 70°nadir angle with the cleanest event class.

To sum up, a statistical significance from the analysis yields 1.38σ. Meaning that there is a confidence level of breaking spectrum in CR proton at 92%. This level of significance is still now strong for confirmation. Nevertheless, the previous study with a few data collection periods gives 1.0σ significant level. It implicitly tells that the larger data collection could increase the statistics and put the weight on the previous study. Surprisingly, the direct CR proton measurement from AMS-02 identify a breaking spectrum at 340 GV which is very close to our work. There is also one plausible assumption where the indirect measurement could not yield a strong significant even we have a huge amount of data.

REFERENCES

1. Abdo, A. A., Ackermann, M., Ajello, M., Atwood, W. B., Baldini, L., Ballet, J., et al. (2009). Fermi large area telescope observations of the cosmic-ray induced γ-ray emission of the earth's atmosphere. *Phys. Rev. D*, 80, 122004.
2. Abdo, A. A., Ackermann, M., Ajello, M., Atwood, W. B., Baldini, L., Ballet, J., et al. (2009). Fermi large area telescope observations of the cosmic-ray induced γ-ray emission of the Earth's atmosphere. *Physical Review D*, 80(12), 122004.
3. Abraham, J., Abreu, P., Aglietta, M., Ahn, E., Allard, D., Allen, J., et al. (2010). Measurement of the energy spectrum of cosmic rays above 1018 ev using the pierre auger observatory. *Physics Letters B*, 685(4-5), 239–246.
4. Ackermann, M., Ajello, M., Albert, A., Allafort, A., Baldini, L., Barbiellini, G., et al. (2014). Inferred Cosmic-Ray Spectrum from Fermi Large Area Telescope γ-Ray Observations of Earth's Limb. *Physical Review Letters*, 112(15), 151103.
5. Ackermann, M., Ajello, M., Allafort, A., Atwood, W. B., Baldini, L., Barbiellini, G., et al. (2012). Measurement of Separate Cosmic-Ray Electron and Positron Spectra with the Fermi Large Area Telescope. *Physical Review Letters*, 108(1), 011103.
6. Adriani, O., Barbarino, G., Bazilevskaya, G., Bellotti, R., Boezio, M., Bogomolov, E., et al. (2009). An anomalous positron abundance in cosmic rays with energies 1.5–100 gev. *Nature*, 458(7238), 607–609.
7. Adriani, O., Barbarino, G., Bazilevskaya, G., Bellotti, R., Boezio, M., Bogomolov, E., et al. (2011). Pamela measurements of cosmic-ray proton and helium spectra. *Science*, 332(6025), 69–72.
8. Aguilar, M., Aisa, D., Alpat, B., Alvino, A., Ambrosi, G., Andeen, K., et al.

(2015). Precision Measurement of the Helium Flux in Primary Cosmic Rays of Rigidities 1.9 GV to 3 TV with the Alpha Magnetic Spectrometer on the International Space Station. *Physical Review Letters*, 115(21), 211101.

9. Aguilar, M., Aisa, D., Alpat, B., Alvino, A., Ambrosi, G., Andeen, K., et al. (2015). Precision measurement of the helium flux in primary cosmic rays of rigidities 1.9 gv to 3 tv with the alpha magnetic spectrometer on the international space station. *Phys. Rev. Lett.*, 115, 211101.
10. Aguilar, M., Aisa, D., Alpat, B., Alvino, A., Ambrosi, G., Andeen, K., et al. (2015). Precision Measurement of the Proton Flux in Primary Cosmic Rays from Rigidity 1 GV to 1.8 TV with the Alpha Magnetic Spectrometer on the International Space Station. *Physical Review Letters*, 114(17), 171103.
11. Amsler, C., et al. (2008). Particle data group. *Phys. Lett. B*, 667(1).
12. Atwater, T. W., & Freier, P. S. (1986a). Meson multiplicity versus energy in relativistic nucleus-nucleus collisions. *Phys. Rev. Lett.*, 56, 1350–1353.
13. Atwater, T. W., & Freier, P. S. (1986b). Meson multiplicity versus energy in relativistic nucleus-nucleus collisions. *Physical review letters*, 56(13), 1350.
14. Atwood, W., Albert, A., Baldini, L., Tinivella, M., Bregeon, J., Pesce-Rollins, M., et al. (2013). Pass 8: Toward the Full Realization of the Fermi-LAT Scientific Potential. *arXiv e-prints*, arXiv:1303.3514.
15. Atwood, W. B., Abdo, A. A., Ackermann, M., Althouse, W., Anderson, B., Axelsson, M., et al. (2009). The Large Area Telescope on the Fermi Gamma-Ray Space Telescope Mission. *The Astrophysical Journal*, 697, 1071–1102.
16. B., R., Ütikofer, E.O., F., & LÜCKIGER (2007). 30th international cosmic ray conference characteristics of near real-time cutoff calculations on a local and global scale.
17. Baldini, L. (2014). Space-based cosmic-ray and gamma-ray detectors: a review. *arXiv preprint arXiv:1407.7631*.

18. Becquerel, H. (1896). On the rays emitted by phosphorescence. *Compt. Rend. Hebd. Seances Acad. Sci.*, 122(8), 420–421.

19. Belolaptikov, I., Budnev, N., Sinegovsky, S., Padusenko, A., Wiebusch, C., Moroz, A., et al. (1997). The baikal underwater neutrino telescope: Design, performance and first results. Tech. rep., SCAN-9704016.

20. Beringer, J., Arguin, J. F., Barnett, R. M., Copic, K., Dahl, O., Groom, D. E., et al. (2012). Review of particle physics. *Phys. Rev. D*, 86, 010001.

21. Bird, D., Corbato, S., Dai, H., Dawson, B., Elbert, J., Emerson, B., et al. (1994). The cosmic-ray energy spectrum observed by the fly's eye. *The Astrophysical Journal*, 424, 491–502.

22. Carlson, A., Hooper, J., & King, D. (1950). Lxiii. nuclear transmutations produced by cosmic-ray particles of great energy.-*Part V.* the neutral mesons. *Philosophical Magazine Series 7*, 41(318), 701–724.

23. Clay, J. (1927). Penetrating Radiation I. In Proceedings of the Royal Academy of Sciences Amsterdam. vol. 30, pp. 1115–1127.

24. Clay, J. (1928). Penetrating Radiation II. In Proceedings of the Royal Academy of Sciences Amsterdam. vol. 31, pp. 1091–1097.

25. Compton, A. H., & Turner, R. (1937). Cosmic rays on the pacific ocean. *Physical Review*, 52(8), 799.

26. Curie, M. (1923). Pierre Curie. Macmillan.

27. De Angelis, A. (2014). Atmospheric ionization and cosmic rays: studies and measurements before 1912. *Astroparticle Physics*, 53, 19–26.

28. Dembinski, H. P., Engel, R., Fedynitch, A., Gaisser, T., Riehn, F., & Stanev, T. (2017). Data-driven model of the cosmic-ray flux and mass composition from 10 GeV to \$10ˆ{11}\$ GeV. In Proceedings of 35th International Cosmic Ray Conference — PoS(ICRC2017). Sissa Medialab.

29. Dermer, C. D., & Powale, G. (2013). Gamma rays from cosmic rays in supernova remnants. *Astronomy & Astrophysics*, 553, A34.

30. Dorman, L. (2009). First measurements of cosmic ray geomagnetic effects and the problem of CR nature. In Astrophysics and Space Science Library, Springer Netherlands. pp. 1–8.

31. Dorman, L. I., Fedchenko, S. G., Granitsky, L. V., & Rishe, G. A. (1970). Coupling and barometer coefficients for measurements of cosmic ray variations at altitudes of 260-400 mb. In International Cosmic Ray Conference. vol. 2, p. 233.
32. Ertley, C. (2014). Studying the polarization of hard x-ray solar flares with the gamma ray polarimeter experiment (grape).
33. Fermi, E. (1949). On the origin of the cosmic radiation. *Physical review*, 75(8), 1169.
34. Fricke, R. G., & Schlegel, K. (2017). Julius elster and hans geitel-dioscuri of physics and pioneer investigators in atmospheric electricity. *History of Geo-and Space Sciences*, 8(1), 1.
35. Gaisser, T. K., Stanev, T., & Tilav, S. (2013). Cosmic ray energy spectrum from measurements of air showers. *Frontiers of Physics*, 8(6), 748–758.
36. Gerward, L. (1999). Paul villard and his discovery of gamma rays. *Physics in perspective*, 1(4), 367–383.
37. Gray, G. W. (1949). Cosmic rays. *Scientific American*, 180(3), 28–39.
38. Greisen, K. (1966). End to the cosmic-ray spectrum? *Physical Review Letters*, 16(17), 748–750.
39. Haino, S., Sanuki, T., Abe, K., Anraku, K., Asaoka, Y., Fuke, H., et al. (2004). Measurements of primary and atmospheric cosmic-ray spectra with the bess-tev spectrometer. *Physics Letters B*, 594(1-2), 35–46.
40. Halzen, F., & Klein, S. R. (2010). Invited review article: Icecube: an instrument for neutrino astronomy. *Review of Scientific Instruments*, 81(8), 081101.
41. Hess, V. F. (1912). Über beobachtungen der durchdringenden strahlung bei sieben freiballonfahrten. *Phys. Z.*, 13, 1084–1091.
42. Huelsenbeck, J. P., & Crandall, K. A. (1997). Phylogeny estimation and hypothesis testing using maximum likelihood. *Annual Review of Ecology and Systematics*, 28(1), 437–466.
43. Hörandel, J. R. (2013). Early cosmic-ray work published in german. *AIP Conference Proceedings*, 1516(1), 52–60.
44. Kachelrieß, M., & Ostapchenko, S. (2012). Deriving the cosmic ray spectrum

from gamma-ray observations. *Phys. Rev. D*, 86, 043004.

45. Kelner, S. R., Aharonian, F. A., & Bugayov, V. V. (2006). Energy spectra of gamma rays, electrons, and neutrinos produced at proton-proton interactions in the very high energy regime. *Physical Review D*, 74(3), 034018.
46. Kennedy, J., & Eberhart, R. (1995). Particle swarm optimization. In Proc. of ICNN'95 - Int. Conf. on Neural Networks. Perth, WA, Australia, vol. 4, p. 1942.
47. Kirk, T. B., & Neddermeyer, S. H. (1968). Scattering of high-energy positive and negative muons on electrons. *Physical Review*, 171(5), 1412.
48. Kolhörster, W. (1934). Cosmic rays under 600 metres of water. *Nature*, 133(3359), 419–419.
49. Kraushaar, W., & Clark, G. (1962). Search for primary cosmic gamma rays with the satellite explorer xi. *Physical Review Letters*, 8(3), 106.
50. Kraushaar, W., Clark, G., Garmire, G., Helmken, H., Higbie, P., & Agogino, M. (1965). Explorer xi experiment on cosmic gamma rays. *The Astrophysical Journal*, 141, 845.
51. Kraushaar, W. L., Clark, G. W., Garmire, G. P., Borken, R., Higbie, P., Leong, V., & Thorsos, T. (1972). High-Energy Cosmic Gamma-Ray Observations from the OSO-3 Satellite. *The Astrophysical Journal*, 177, 341.
52. Lesur, V. (2006). Introducing localized constraints in global geomagnetic field modelling. *Earth, planets and space*, 58(4), 477–483.
53. Linsley, J. (1963). Evidence for a primary cosmic-ray particle with energy 10 20 ev. *Physical Review Letters*, 10(4), 146.
54. Maldera, S. (2019). Fermi-lat performance,. `https://www.slac.stanford.edu/exp/glast/groups/canda/lat_Performance.htm`. Accessed: 2021-04-19.
55. Michelson, P. F., Atwood, W. B., & Ritz, S. (2010). Fermi gamma-ray space telescope: high-energy results from the first year. *Reports on Progress in Physics*, 73(7), 074901.

56. Millikan, R. A. (1932). Cosmic-ray ionization and electroscope-constants as a function of pressure. *Physical Review*, 39(3), 397.

57. Morris, D. J. (1984). Production of high-energy gamma rays by cosmic ray interactions in the atmosphere and lunar surface. *Journal of Geophysical Research*, 89, 10685–10696.

58. Morrison, P. (1958). On gamma-ray astronomy. *Il Nuovo Cimento (1955-1965)*, 7(6), 858–865.

59. Neddermeyer, S. H., & Anderson, C. D. (1937). Note on the nature of cosmic-ray particles. *Physical Review*, 51(10), 884.

60. Nuntiyakul, W., Evenson, P., Ruffolo, D., Sáiz, A., Bieber, J. W., Clem, J., et al. (2014). Latitude Survey Investigation of Galactic Cosmic Ray Solar Modulation during 1994-2007. *The Astrophysical Journal*, 795, 11.

61. Orth, C. D., & Buffington, A. (1976). Secondary cosmic-ray electrons and positrons from 1 to 100 gev in the upper atmosphere and interstellar space, and interpretation of a recent positron flux measurement. *The Astrophysical Journal*, 206, 312–332.

62. Petry, D. (2005). The Earth's Gamma-ray Albedo as observed by EGRET. In F. A. Aharonian, H. J. Völk, & D. Horns (Eds.), High Energy Gamma-Ray Astronomy. *American Institute of Physics Conference Series*, vol. 745, pp. 709–714.

63. Rochester, G., & Butler, C. (1953). The new unstable cosmic-ray particles. *Reports on Progress in Physics*, 16(1), 364.

64. Rossi, B. (1930). On the Magnetic Deflection of Cosmic Rays. *Physical Review*, 36, 606–606.

65. Rossi, B., & Greisen, K. (1941). Cosmic-ray theory. *Reviews of Modern Physics*, 13(4), 240.

66. Ruffolo, D., Sáiz, A., Mangeard, P.-S., Kamyan, N., Muangha, P., Nutaro, T., et al. (2016). Monitoring Short-term Cosmic-ray Spectral Variations Using Neutron Monitor Time-delay Measurements. *The Astrophysical Journal*, 817, 38.

67. Shea, M., Smart, D., & McCracken, K. (1965). A study of vertical cutoff

rigidities using sixth degree simulations of the geomagnetic field. *Journal of Geophysical Research*, 70(17), 4117–4130.

68. Sigl, G. (2012). High energy neutrinos and cosmic rays. *arXiv preprint arXiv:1202.0466*.
69. Skobeltzyn, D. (1929). The Angular Distribution of Compton Recoil Electrons. *Nature*, 123(3098), 411–412.
70. Skobeltzyn, D. V. (1985). The early stage of cosmic ray particle research. In Early History of Cosmic Ray Studies, Springer. pp. 47–52.
71. Stecker, F. W. (1973). Simple Model for Scanning-angle Distribution of Planetary Albedo Gamma-rays. *Nature Physical Science*, 242, 59–60.
72. Stephens, S. A., & Badhwar, G. D. (1981). Production spectrum of gamma rays in interstellar space through neutral pion decay. *Astrophysics and Space Science*, 76, 213–233.
73. Störmer, C. (1934). Critical remarks on a paper by g. lemaître and ms vallarta on cosmic radiation. *Physical Review*, 45(11), 835.
74. Svensson, G. (1958). The cosmic ray photon and π^0-meson energy spectra at 29-30 km above sea-level. *Arkiv Fysik*, 13, 347.
75. Taylor, A. M. (2016). Cosmic rays beyond the knees. *Nature*, 531(7592), 43–44.
76. Thébault, E., Finlay, C. C., Beggan, C. D., Alken, P., Aubert, J., Barrois, O., et al. (2015). International geomagnetic reference field: the 12th generation. *Earth, Planets and Space*, 67(1), 79.
77. Thompson, D. J., Simpson, G. A., & Ozel, M. E. (1981). SAS 2 observations of the earth albedo gamma radiation above 35 MeV. *Journal of Geophysical Research*, 86, 1265–1270.
78. Trenn, T. J. (1976). Rutherford on the alpha-beta-gamma classification of radioactive rays. *Isis*, 67(1), 61–75.
79. Tsyganenko, N. A. (1987). Global quantitative models of the geomagnetic field in the cislunar magnetosphere for different disturbance levels. *Planetary and Space Science*, 35, 1347–1358.
80. Van Allen, J. A., & Frank, L. A. (1959). Radiation around the earth to a radial distance of 107,400 km. *Nature*, 183(4659), 430–434.

81. Van Oosterom, A., & Strackee, J. (1983). The solid angle of a plane triangle. *IEEE Transactions on Biomedical Engineering*, BME-30(2), 125–126.

82. Wallace, J. M., & Hobbs, P. V. (2006). Atmospheric. Science.

83. Watson, A. (2000). Ultra-high-energy cosmic rays: the experimental situation. *Physics Reports*, 333, 309–327.

84. Wilks, S. S. (1938). The large-sample distribution of the likelihood ratio for testing composite hypotheses. *Ann. Math. Statist.*, 9(1), 60–62.

85. Wilson, C. T. R. (1921). Iii. investigations on lighting discharges and on the electric field of thunderstorms. *Philosophical Transactions of the Royal Society of London. Series A, Containing Papers of a Mathematical or Physical Character*, 221(582-593), 73–115.

86. Yoshida, S., Hayashida, N., Honda, K., Honda, M., Imaizumi, S., Inoue, N., et al. (1994). Lateral distribution of charged particles in giant air showers above 1 eev observed by agasa. *Journal of Physics G: Nuclear and Particle Physics*, 20(4), 651.

APPENDICES

APPENDIX A
TESTING THE EXPOSURE MAP

APPENDIX B
POWER LAW IN ENERGY

APPENDIX C
SUBTRACTING γ-RAY BACKGROUND

blabla

APPENDIX D
INTERACTION MODEL

BIOGRAPHY

NAME	Mr. Patomporn Payoungkhamdee
DATE OF BIRTH	29 April 1996
PLACE OF BIRTH	Bangkok, Thailand
INSTITUTIONS ATTENDED	Mahidol University, 2014–2017 Bachelor of Science (Physics) Mahidol University, 2018–2020 Master of Science (Physics)
HOME ADDRESS	86/46 Moo. 7, Bangmuang, Muang, Samutprakan 10270 Thailand
E-MAIL	patomporn.pay@student.mahidol.ac.th